Journal Pre-proofs

Influence of mixed-phase TiO$_2$ on the activity of adsorption-plasma photocatalysis for total oxidation of toluene

Zhiping Ye, Zhen Ye, Anton Nikiforov, Jun Chen, Wu Zhou, Jianmeng Chen, Guanjie Wang, Yufen Zhang

Please cite this article as: Z. Ye, Z. Ye, A. Nikiforov, J. Chen, W. Zhou, J. Chen, G. Wang, Y. Zhang, Influence of mixed-phase TiO$_2$ on the activity of adsorption-plasma photocatalysis for total oxidation of toluene, *Chemical Engineering Journal* (2020), doi: https://doi.org/10.1016/j.cej.2020.126280

This is a PDF file of an article that has undergone enhancements after acceptance, such as the addition of a cover page and metadata, and formatting for readability, but it is not yet the definitive version of record. This version will undergo additional copyediting, typesetting and review before it is published in its final form, but we are providing this version to give early visibility of the article. Please note that, during the production process, errors may be discovered which could affect the content, and all legal disclaimers that apply to the journal pertain.

Influence of mixed-phase TiO$_2$ on the activity of adsorption-plasma photocatalysis for total oxidation of toluene

Zhiping Ye [a], Zhen Ye [a], Anton Nikiforov [b], Jun Chen [a], Wu Zhou [a], Jianmeng Chen [a,*], Guanjie Wang [a], and Yufen Zhang [a]

[a] College of Environment, Zhejiang University of Technology, 310014 Hangzhou, PR China

[b] Ghent University, Faculty of Engineering, Department of Applied Physics, Research Unit Plasma Technology, Sint-Pietersnieuwstraat 41, 9000 Ghent, Belgium

* Corresponding author

E-mail: jchen@zjut.edu.cn (J. Chen)

Keywords: Adsorption-Plasma Photocatalysis, Mixed-phase TiO$_2$, plasma-photocatalytic mechanism, Emission spectroscopy, Reaction pathway

Abstract:

Herein, the effects of different crystalline phases of TiO_2 on the adsorption-plasma photocatalytic oxidation of toluene were investigated. First, photocatalysts loaded on a molecular sieve (MS) were characterised and the catalytic performance of toluene abatement was evaluated in a plasma system. The CO_X yield of the pure anatase (An) sample outperformed other samples in the adsorption-plasma photocatalytic oxidation process, especially for CO_2 yield (69.1%). It was revealed that the highest space-time-yield of 2.35 g_{CO_2}/Lcat•h was also achieved using plasma-An/MS. However, the highest total toluene abatement (99.5%) was achieved in the plasma-P25/MS system. The plasma-generated UV flux only played a minor role in photocatalyst activation because of the very low UV flux of 2.7 $\mu W/cm^2$ generated by discharge. For the degradation pathway, compared with the plasma-MS system, byproducts of 1,3-Butadiyne (C_4H_2), guanidine, methyl- ($C_2H_7N_3$) did not exist in the TiO_2-assisted system, indicating a difference in the toluene degradation pathway. There were no obvious effects of different TiO_2 samples on organic byproducts generation, and almost a complete mineralisation of all byproducts was observed after 30 min of treatment, with the exception of ethylamine (C_2H_7N) and acetaldehyde (C_2H_4O). Finally, a cycled adsorption-plasma study was conducted to reveal the sustainability of the process. A partial deactivation of plasma-An/MS with less than 7% decrease in CO_2 selectivity after 7 cycles was revealed, which is a promising result for use in possible industrial applications.

1. Introduction

Presently, toluene is one of the most important chemicals in industry due to its extensive applicability many areas, including petrochemicals and coatings, however, the adverse effects of toluene can directly cause serious harm to human health and indirectly act as a precursor of tropospheric ozone/photochemical smog [1, 2]. Hence, the removal of toluene has become of great interest. Among volatile organic compounds (VOCs) removal techniques, plasma-photocatalysis is a promising method due to its high pollutant removal efficiency, CO_2 selectivity, low production of byproducts, and high energy efficiency [3-7].

As of late, the optimisation process of plasma-photocatalysis for VOCs abatement has been gaining increasing attention to researchers. With a focus regarding important parameters that affect the plasma-photocatalysis process, studies have been conducted on: *i*) catalyst properties (morphology and structure) [8-10]; *ii*) the discharge reactor configuration, including dielectric barrier discharge (DBD) [11, 12] and surface discharge barrier dielectric (SDBD) [13, 14]); *iii*) and methods of discharge excitation [6, 15, 16]. Further, a large number of studies were directed toward the influence of different adsorbents for doping catalysts loaded on Al_2O_3 support, molecular sieve (MS), Zeolite Socony Mobil–5 material (ZSM-5) [16-18], TiO_2 modified (nano) TiO_2/SMF (sintered metal fibre) [19], graphene-TiO_2 [20], noble metals (Ag, Pt, or Pd)/TiO_2 [19, 21, 22], and non-noble metals (MnO_X, SnO_2, or Ce-Mn)/TiO_2 [6, 23-25]). Moreover, an improved VOCs abatement combining the plasma and photocatalysts processes was observed by various researchers, but the mechanisms of the plasma-induced photocatalytic reactions require further clarity. It was reported that plasma-generated UV photons were able to create electron-hole pairs of TiO_2 catalysts for VOCs oxidation [10]. Conversely, the UV flux in a typical dielectric barrier

air discharge was observed at several $\mu W/cm^2$ [26], while the UV flux generated by UV lamps is usually many orders of magnitude larger, thus, the contribution of plasma-generated UV flux was believed to be negligible in many works [27].

Therefore, our first objective was to investigate the role of UV flux generated in the plasma during catalyst activation. Considering that TiO_2 is a well-known photocatalyst, the associated of the nature of a photocatalyst (physical, chemical, and optical properties) on the plasma-photocatalytic oxidation of toluene are a topic of interest. TiO_2 is an excellent photocatalyst, and has three different crystal forms (anatase, rutile and brookite). Anatase, which has a band gap of 3.2 eV, is commonly used as a photocatalyst [28, 29]. As the direct band gap of rutile is only 3.02 eV [30] and its photocatalytic activity is lower than that of anatase, it is not used as often. A well-known photocatalyst P25 is a mixed-phase titanium photocatalyst. Tobaldi et al. found P25 to be composed of 76.3% anatase, 10.6% rutile, and 13.0% amorphous phases [31]. Apopei et al. reported that Degussa P25 is a mixture of anatase and rutile, with a ratio of 78 wt.% anatase, 14 wt.% rutile, and 8 wt.% amorphous TiO_2 [30]. It has been reported that P25 mixed-phase TiO_2 photocatalysts comprised of both anatase and rutile microcrystals display higher photo-activity than single-phase TiO_2 [30]. Therefore, it is necessary to examine how different crystalline phases of TiO_2 affect the plasma-catalytic oxidation of toluene.

Hence, in this study TiO_2 incorporated into a MS is investigated using different formulations of the aforementioned materials, such as single-phase TiO_2 in (An (anatase) and Ru (rutile)) form, mechanical mixture of An to Ru in the ratio of 3:1, and commercial P25. Further, we investigated the effect of different crystalline phases of TiO_2 on the carbon balance in the plasma-catalytic system. We also investigated how to select the appropriate TiO_2 crystalline phase as it is critical in

the application process. Further, we evaluated the influence of different TiO_2 phases on byproduct generation following the toluene degradation pathways.

Meanwhile, in order to understand the interactions between plasma and TiO_2, the physicochemical properties of catalysts before and after discharge were intensively characterised by X-ray diffraction (XRD), scanning electron microscopy (SEM), Brunner-Emmet-Teller (BET) measurements, X-ray photoelectron spectroscopy (XPS), and UV–vis diffuse reflectance absorption spectra (DRS). Moreover, plasma diagnostic methods were applied for the analysis of plasma properties and discharge waveforms of plasma combined with catalysts.

2. Experimental

2.1 Preparation of the catalysts

2.1.1 Isolation process

The isolation of anatase and rutile powder from commercial P25 (Maclean, China) was adapted by the method described by Apopei et al. [30]. The materials obtained from this treatment are denoted as An and Ru. The single-phase An was isolated by dissolving of 4 g P25 in 400 mL of hydrogen peroxide (30%) (AR, Maclean, China), and 40 mL ammonium hydroxide (2.5%) (AR, Maclean, China). This solution was stirred (500 rpm) for 24 h at room temperature (approximately 25 °C), and the resultant colloidal precipitate was centrifuged and extensively washed with deionised water, and was then dried at 60 °C for 24 h. The Ru sample was obtained using HF solution (10%) (AR, Maclean, China)for dissolution of anatase parts in P25. The solid product was prepared in a same method with the An sample.

2.1.2 Synthesis of TiO$_2$/MS

The TiO$_2$-catalyst loaded MS (2-3 mm, Maclean, China) samples were prepared using an impregnation method wherein 0.1 g of powder catalyst (An, Ru, P25, and 3An:1Ru, which has a 3:1 weight ratio of An to Ru) and 20 g of MS were immersed in 80 mL of absolute ethanol solution. After stirring for 3 h at room temperature (approximately 25°C), the mixture was stirred at 50°C in a rotary evaporator (80 rpm, 250 mbar) (R-215, Buchi, Switzerland) until the sample was dry. Then, it was kept in an oven at 60°C for 24 h. The resulting materials were calcined at 300°C for 2 h in air with a temperature gradient of 5°C/minute. Finally, the obtained catalysts were labeled as An/MS, Ru/MS, P25/MS, and 3An:1Ru/MS.

2.2. Catalyst characterisation

Ti elemental composition analyses were performed using inductively coupled plasma-optic emission spectroscopy (ICP-OES) (Optima 2100DV, Perkin Elmer, USA). The XRD patterns of the samples were recorded on a X' Pert PRO diffractometer using Cu Kα X-ray radiation with a 0.02° step size over the 2-theta range: 10° – 80°. The morphologies of catalysts were examined using SEM (S-4700, Hitachi, Japan). Before SEM analysis, the samples were coated with Au via an E-1030 Ion Sputter in order to avoid charge effects. XPS with a monochromatic Al Kα source was employed to study the surface properties and valence state distribution (ESCALAB 250Xi, Thermo, USA), and the C 1s level at 284.8 eV was regarded as an internal standard to revise the shift of the binding energy due to relative surface charging. The DRS were recorded using a UV–vis spectrophotometer (U-3900H, Hitachi, Japan). Thermal gravimetric (TG) analysis was

performed using a thermogravimetric analyser (TGA-SDTA 851e, Mettler, Switzerland) at a heating rate of 10°C/min up to 750°C. A vector network analyser (VNA) (N5245A, Agilent, USA) was used to measure the dielectric constant of the materials at 2 – 18 GHz. Finally, to obtain the best estimate of the band gap energy, the absorbance data was first shifted such that the minimum value was set to zero to account for any wavelength independent reflectance and scattering [32]. Then, a line tangent to the slope in the linear region of the absorption onset was drawn, and the intersection of the two lines corresponds to the best estimate for the energy of the band gap.

$$h\nu \text{ (eV)} = (1240.8 \text{ (eV*nm))} / (\lambda(nm)) \qquad (1)$$

$$\alpha h\nu = (h\nu - Eg)^{1/n} \qquad (2)$$

The Tauc plots of $(\alpha h\nu)^n$ versus $h\nu$ yield the value of the band gap when extrapolated to the baseline, wherein n can take on values of 2 or 1/2, corresponding to direct and indirect transitions, respectively.

2.3 Experimental set-up and procedure

Fig. 1 shows the schematic diagram of the experimental set-up including (1) a plasma-catalysis reactor (A) and photocatalytic reactor (B), (2) the reaction gas supply system, and (3) the gas analysis instrumentation.

Toluene (99.99% purity, Maclean, China) was evaporated by bubbling with dry air and diluted with dry air before being introduced into the plasma reactor. The flow rate and toluene

concentration were adjusted by mass flow controllers (MFC) and fixed at 2 L/min and ~153 mg/m^3, respectively.

The discharge of the packed bed DBD plasma reactor was generated in a vertically oriented 400 mm long coaxial quartz cylinder that had an inner diameter of 19 mm and wall thickness of 3 mm. The inner high voltage electrode was a stainless-steel rod with a diameter of 5.6 mm, while a copper sheet with a thickness of 0.05 mm and length of 50 mm was placed on the outer surface of the quartz tube to act as a ground electrode. The discharge gap between the two parallel electrodes was filled with approximately 4.5 g of spherical particle samples with a diameter of 2 – 3 mm, and was placed in the middle of the copper sheet using quartz wool.

The UV reactor was composed of a quartz tube (length 196 mm, inner diameter 28 mm, outer diameter 32.3 mm) and a UV lamp (Cnlight ZW8S15W-Z287 8D01: outer diameter 15 mm, length 287 mm, power of 8 W, main wavelength 365 nm). This lamp was placed in the middle of the quartz tube, and the two ends were sealed with a joint of polytetrafluoroethylene.

The toluene degradation performance of different crystal catalysts in the plasma system was studied in the following order: (i) during the adsorption phase, the inlet concentration of toluene was ~153 mg/m^3 with the total flow rate of 2 L/min. The amount of catalyst was ~4.5 g with the packing length of ~2.5 cm. The filling volume of the catalyst in the DBD reactor was ~6.47 cm^3, resulting in a space velocity of 18547 h^{-1}. Adsorption reached equilibrium when the inlet and outlet concentrations of the toluene were nearly equal; (ii) then, the toluene containing gas stream was stopped; (iii) in the discharge phase, 100 mL/min of pure dry air was passed into the reactor for a 90 min discharge. Toluene and CO_X (CO and CO_2) concentrations were analysed using a gas

chromatograph (7890, Agilent, USA) equipped with two detectors: a flame ionisation detector (HP-INNOWAX column), and a thermal conductivity detector (HP-PLOT/Q column). Ozone formation was analysed by an ozone monitor (106-MH, 2B Technologies, USA). The Model 42i NOx Chemiluminescence analyser was used for detecting nitrogen oxides (NO_2 and NO) in the exhaust gas, and a GC–MS instrument (7890A-5975C, Agilent, USA) equipped with a DB-5MS column was used to identify the byproducts generated in different discharge time periods. To assess the performance of the proposed catalysts, the key performance metrics, such as total toluene adsorption, total toluene removal efficiency (TRE), CO yield, CO_2 yield, optical property of catalyst, catalyst dosage, space-time-yield (STY), and specific energy (SE), were used. The calculation formulas are as follows:

$$\text{Adsorption capacity (mg/g)} = \frac{\int_0^{t_1} Q_1([C_7H_8]_{inlet} - [C_7H_8]_{outlet})dt}{catalyst\ dosage\ (g) \times 1000}, \tag{3}$$

$$n_{C_7H_8}^{adsorbed}\ (mmol) = \frac{\int_0^{t_1} Q_1([C_7H_8]_{inlet} - [C_7H_8]_{outlet})dt}{M_{C_7H_8} \times 1000}, \tag{4}$$

$$n_{C_7H_8}^{desorbed}(mmol) = \frac{\int_0^{t_1} Q_2([C_7H_8]_{desorbed})dt}{M_{C_7H_8} \times 1000}, \tag{5}$$

$$n_{CO_2}\ (mmol) = \frac{\int_0^{t_2} Q_2[CO_2]dt}{M_{CO_2} \times 1000}, \tag{6}$$

$$n_{CO}(mmol) = \frac{\int_0^{t_2} Q_2[CO]dt}{M_{CO} \times 1000}, \tag{7}$$

$$\text{TRE (\%)} = \frac{n_{C_7H_8}^{adsorbed} - n_{C_7H_8}^{desorbed}}{n_{C_7H_8}^{adsorbed}} \times 100, \tag{8}$$

$$Y_{CO_2}\ (\%) = \frac{n_{CO_2}}{7 \times n_{C_7H_8}^{adsorbed}} \times 100, \tag{9}$$

$$Y_{CO}\ (\%) = \frac{n_{CO}}{7 \times n_{C_7H_8}^{adsorbed}} \times 100, \tag{10}$$

$$\text{SE (kJ/L)} = \frac{P \times 60}{Q_2 \times 1000}, \tag{11}$$

$$\text{STY (g/L/h)} = \frac{[\int_0^{t_2} Q_2 [CO_2] dt] \times 60}{V_{cat} \times t_2 \times 1000}, \tag{12}$$

where $n_{C_7H_8}^{adsorbed}$ and $n_{C_7H_8}^{desorbed}$ are the amount of toluene adsorbed on the catalyst and the amount of desorbed toluene (mmol), respectively, n_{CO_2} and n_{CO} are the total amount of CO_2 and CO produced during discharge, respectively, M is the molar mass of the molecule (g/mol), V_{cat} is the filled volume of the catalyst (L), Q_1 and Q_2 are the flow rates (L/min) during the adsorption and discharge processes, respectively, t_1 and t_2 are adsorption equilibrium time (min) and discharge time, respectively, $[C_7H_8]_{inlet}$ and $[C_7H_8]_{outlet}$ are the inlet and outlet concentrations, respectively, of toluene (mg/m^3) at the adsorption stage, $[CO_2]$ is the CO_2 concentrations (mg/m^3) in the gas stream during plasma catalytic process, P (W) is the input power as measured by oscilloscope, and SE (kJ/L) is the specific energy. An AC high voltage with a 22 kV peak to peak voltage and a fixed frequency of 9.0 kHz was applied to the inner electrode, while the outer electrode was connected to the ground. The applied voltage was measured using a 1000:1 high voltage probe (P6015A, Tektronix, USA) while the discharge current was monitored by a current probe (TCP0030, Tektronix, USA). The instantaneous voltage (V(t)) and current (I(t)) waveforms were recorded using a digital oscilloscope (DPO3012, Tektronix, USA). The excited radiative species generated in the discharge were monitored using OES in the UV/VIS range of the spectrum as OES is the most common technique used in plasma diagnostics, especially, in the UV- visible region for determining vibrational and rotational distribution functions of electronically excited states in molecular plasmas [33, 34]. The light emission spectrum was collected by an optical fibre (SMA905) positioned a few millimetres from the discharge region at an angle of approximately

30° in the direction of the quartz tube axis. The discharge spectra calibrated for relative sensitivity were recorded in the spectral range 250 – 800 nm using a 750 mm Triple Grating Imaging Spectrometer (Spectrapro SP-2750, Princeton, USA) with a resolution of 0.023 nm. The presence of molecular bands of the N_2 transition $C^3\Pi_u$-$B^3\Pi_g$ in the emitted spectra allows for the estimation of rotational and vibrational temperatures (T_{rot} and T_{vib}, respectively) of the N_2 molecule. Due to the high frequency of the particle's collisions (at the working pressure), the rotational temperature of N_2 is equivalent to the gas temperature. Gas temperature is one of the key parameters for technological application, therefore, special attention must be paid to optimise the energy required for the heating. Herein, three bands: Δv=1 (1-0, 2-1, 3-2), Δv=-1(0-1, 1-2, 2-3), and Δv=-2 (0-2, 1-3, 2-4) were used to first estimate the T_{vib}. The T_{vib} of the N_2 molecular has already been determined by means of the algorithm presented in [35]. The T_{rot} was determined by analysis of the rotational structure of nitrogen molecular bands in the second positive system, namely the 0-0 vibrational band of N_2 ($C^3\Pi_u$-$B^3\Pi_g$) emission at λ = 337.1 nm. The synthetic spectrum calculated by the Specair 2.2 program was compared to our experimental results. The best fitting among the spectra was found by varying T_{rot} while keeping T_{vib} constant. The same procedure has been used by different groups, e.g. Nassar [36], and the estimated uncertainty of the method is 150 K for T_{rot} and 500 K for T_{vib}.

OES can also be used to determine the electrical field strength in air plasmas at atmospheric pressure [37, 38]. The excitation energy of the N_2 ($C^3\Pi_u$, $v = 0$) and N_2^+ ($B^2\sum_u^+$, $v = 0$), which belong to the second positive system of N_2 ($C^3\Pi_u \rightarrow B^3\Pi_g$) and the first negative system of N_2^+ ($B^2\sum_u^+ \rightarrow X^2\sum_g^+$), are 11.03 eV and 18.7 eV, respectively. This significant energy difference causes their intensity ratio to be quite sensitive to electron energy and, consequently, to the

reduced electrical field. In the approximation, the excitation mechanism of the N_2 ($C^3\Pi_u$) and N_2^+ ($B^2\sum_u^+$), occour only by direct electron impact, as is always the case for DBD plasmas [39]. Then, the reduced electrical field can be estimated from a ratio of line intensity at 337 nm and 391 nm. Paris et al. [40] applied this method in a wide pressure range, from 300 Pa to 10^5 Pa, for air discharges. Their approach, which was based on electron impact excitation was applied to estimate the electric field. Herein, the radiative lifetime and deactivation rate constants due to quenching of N_2 radiative states were assumed to be the same as in [40].

3. Results and discussion

3.1. Characterisation of the titanium dioxide samples

The powder XRD patterns are illustrated in Fig. 2. The main diffraction peaks at 25.2°, 37.8°, and 48.0° were found to be associated with the anatase crystalline phase by comparing them with the JCPDS database (JPCDS, 21-1272), and the peaks at 27.4°, 36.0°, and 54.3° represent the characteristic pattern of the rutile phase (JPCDS, 21-1276) [20]. For the commercial P25 and 3An:1Ru, the coexistence of the anatase and rutile phases were indexed. The phases in the P25 sample exhibited more intense and narrower peaks compared with other samples, suggesting the P25 had a larger particle size and higher crystallinity [41]. Note that when the prepared TiO_2 samples were doped on the MS support, some of the characteristic reflections of the anatase or rutile phases were shadowed by the peaks of the MS (Fig. S1), which might have been caused by the relative low content of TiO_2 and high dispersion of TiO_2 within the hybrid composites [20, 41]. The surface morphology of the titanium samples is shown in Fig. 3. The SEM images for An and

Ru clearly show the uniform spherical grains grouped in randomly aggregated particles, with an average particle size in the range of 30 – 40 nm. Meanwhile, the commercial P25 sample shows the surface morphology of a larger quasi-spherical shape in the range of 50 – 70 nm, which is in agreement with the XRD results. Further, it can be observed that the surface morphology of 3An:1Ru is similar to that of P25.

The elemental compositions of the MS-supported TiO_2 catalysts are summarised in Table S1. The Ti wt.% of all the TiO_2/MS samples were similar at approximately 0.39 wt.%. Table S1 also summarises the textual properties of the samples. The surface area difference between the MS and supported-MS samples is not significant (Table S1), which may be due to the low amount of TiO_2 catalyst loaded on the MS surface (~0.39 wt.%). Although the larger specific surface area is believed to achieve higher adsorption capacities, the relationship of specific surface area and adsorption capacity is not an absolute positive correlation [17] as the adsorption capacity could also be affected by the gas flow rate, adsorption time, and toluene concentration. The adsorption equilibrium curves of the samples are shown in Fig. S2. Note that the adsorption capacities of the MS and supported-MS samples in this study (~2.1 mg/g) are much higher than the results of Lin et al. [17], even though similar surface areas of MS were used in both. This suggests that the adsorption capacities of the samples were not limited by the specific surface area. Moreover, the experimental results show that the adsorption capacities of the samples were not very different.

The XPS spectral information is displayed in Fig. 4. Based on the spectra collected, we investigated the chemical compositions and defects of titanium oxides on MS. Ti^{3+} was observed on the surfaces of many different catalysts, and the Ti $2p_{3/2}$ and Ti $2p_{1/2}$ peaks of Ti^{3+} were located at approximately 457.7 eV and 463.8 eV, respectively, which the Ti $2p_{3/2}$ and Ti $2p_{1/2}$ peaks

located at 458.3 eV and 464.7 eV, respectively, were assigned to the typical Ti^{4+} characteristics [42]. Meanwhile, the O 1s peak of the TiO_2 samples could be deconvoluted into five different O peaks. The peaks at 529.5 eV, 530.5 eV, 531.2 eV, 532.2 eV and 533.2 eV were assigned to the typical $O-Ti^{4+}$, $O-Ti^{3+}$, surface hydroxyl oxygen (Sur-OH), vacancy oxygen (V_O), and adsorption O, respectively [20, 43]. The presence of Ti^{3+} was believed to form the V_O on the catalyst surface ($2Ti^{4+} + O^{2-} \rightarrow V_O + 2Ti^{3+} + 1/2O_2$, where O^{2-} is the lattice oxygen) [20]. In addition, the atomic concentration ratios of $Ti^{3+}/(Ti^{3+} + Ti^{4+})$ were calculated according to the areas under separate deconvolution curves, which are listed in Table 1. The highest ratio of Ti^{3+} to $Ti^{3+}+Ti^{4+}$ reached 34.49% on the surface of the P25/MS sample, which had the highest V_O ratio. Therefore, when a catalytic test is performed, the highest CO_2 yield is expected to be achieved using P25/MS in the photocatalytic degradation process (Fig. S3) as a result of the V_O acting as the active site preventing recombination of $e^- - h^+$ pairs in photocatalytic reactions [3]. The photocatalytic performance of the samples were found to follow the order of the V_O ratio. Note that for 3An:1Ru, the mechanical mixture of anatase and rutile could not compete with P25 in CO_2 yield. The P25 was composed of the anatase phase (78%), rutile phase (14%), and amorphous (8%), wherein the integrated rutile phase helped to improve the carriers separation by trapping electrons, benefiting the photocatalysis process [30]. The discrepancy between samples reflects the influence of crystalline structures on controlling photocatalytic activity.

The effect of a crystalline phase on the light absorption range and band gap was investigated. As seen in Fig. 5a, the UV–vis spectrums of all the samples show no absorption in the non-UV region of more than 400 nm, except for the Ru sample. The visible light absorbance of the Ru sample slightly increased, shifting toward red wavelengths, which is similar to the results reported by

Schulte et al. [44]. This could assist the photocatalytic activity of the Ru sample in the plasma discharge process without UV light irradiation. Meanwhile, compared to P25 and 3An: 1Ru, the light absorption peaks of the isolated An and Ru samples were higher in the UV region, indicating a better utilisation efficiency in the UV region. This may explain the better catalytic performance of isolated An and Ru samples than that of the 3An:1Ru sample. However, note that all the key physicochemical properties of TiO_2, such as crystal phase, crystallite size, surface area, and band gap, could also affect the photocatalytic activity [45]. Unlike the 3An:1Ru sample, the P25 sample exhibited a promising toluene degradation in the plasma system, which may be due to the special crystal structure involving amorphous phases [44]. According to Tauc's equation [32], the optical direct and indirect band-gap energies of the samples were summarised (Figs. 5 (b, c) and Table 2). The indirect band gap of An was approximately 3.18 eV, implying a strong redox ability [44, 46]. For Ru, the band gap values located in the range of 2.98 – 3.10 were independent of the plot type (direct or indirect). The optical direct and indirect band-gap energies of 3An:1Ru were 3.28 eV and 3.02 eV, respectively, which are located between the single-phase An and Ru.

3.2. Adsorption-discharge performance of the samples

The carbon balances of the commercial catalyst and three prepared catalysts were investigated. As seen in Fig. 6 and Table 2, the initial toluene concentration was fixed at ~ 153 mg/m^3 and the input energy of plasma discharge was ~13.1 W when the catalytic performances were compared. It is clear that TiO_2 supported catalysts promoted the yield of CO_X (CO_2 + CO) as CO_X yields of the

plasma-photocatalysis system were above 80% compared with only ~45% of CO_X yield using the plasma-MS system. For CO_2 yield, more toluene was completely oxidised into CO_2 using photocatalysts than that of the MS system. Further, the pure An sample outperformed the Ru sample in CO_2 yield, which was as expected. The sample of 3An:1Ru did not exhibit an enhanced synergistic effect from its mixed-phase as compared to the single-phase samples in the plasma-photocatalysis system, while the CO_2 yield of P25 was comparable to the single-phase samples where the lowest toluene remaining was observed in the P25 sample. The total toluene removal efficiencies are summarised in Table 2, Note that, the removal of toluene could be highly efficient (**> 95%**) at an input energy of ~13.1 W, regardless of system used. However, the highest total toluene abatement of 99.5% was achieved in the plasma-P25 system. Based on the OES analysis results (Table 3), the average electric field in the plasma P25/MS discharge is 670×10^{-21} Vm^2. Among the toluene abatement reactions, the electron impact reactions were considered to be the main causes of toluene removal [47]. This may suggest that more high-energy electrons were generated for toluene abatement in the plasma-P25/MS system, which may help explain the resultant carbon balance with the least residual toluene. However, it must be clarified that partial toluene was degraded into other carbonaceous compounds (Fig. 6). Herein, it was revealed that ~48.9% of toluene turned into organic carbonaceous byproducts in the plasma-MS system. The composition of byproducts is discussed in Section 3.4. In order to evaluate the catalytic performance of the samples, the STY of CO_2 were calculated (Table 2). The STY of An/MS, Ru/MS, P25/MS, 3An:1Ru/MS, and MS were 2.35 g_{CO2}/Lcat·h, 2.09 g_{CO2}/Lcat·h, 2.16 g_{CO2}/Lcat·h, 2.0 g_{CO2}/Lcat·h and 1.31 g_{CO2}/Lcat·h, respectively. Therefore, the photocatalysts did promote the toluene conversion into CO_2. This suggests that the photocatalytic oxidation process

induced by discharge may occur in the plasma system even without additional light irradiation. Note that the mechanical mixing of An and Ru did not enhance the STY.

3.3. Plasma−photocatalytic interactions

The influence of catalysts tested in a plasma discharging system on discharge properties was studied. In terms of the relative permittivity of various TiO_2 and the relative complex permittivity of TiO_2/paraffin composite were analysed using a VNA. Fig. 7 depicts the variation of dielectric constant (ϵ') and dielectric loss tangent (ϵ''/ ϵ') of titanium samples against increasing frequency. For every sample, the value of ϵ' tends to decrease with increasing frequency. This may be a result of the dipole polarisation independence of the rapidly varying electric field at large frequencies [48]. Meanwhile, the value of ϵ' decreases in the order of P25/MS, An/MS, 3An:1Ru/MS, to Ru/MS, which is in agreement with the values of the electric field of all the catalysts. Conversely, Fig. 7b shows that the dielectric loss tangent followed the order of P25/MS, 3An:1Ru/MS, An/MS, to Ru/MS, showing that the mixed-phases titanium oxides converted more consumed energy into heat energy than isolated TiO_2.

It was revealed that the discharge behaviour was affected by the properties of different crystalline phases. A less stable discharge with a lower discharge current was produced for the MS-packed discharge, as seen inside of red square in Fig. 8, implying a relatively unstable discharge compared with that of the TiO_2 supported sample. Ultimately, this leads to less effective plasma reactions, resulting in poor carbon balance performance. A continuous relatively high current was observed for the P25/MS packed discharge, which may be caused by the higher relative dielectric

permittivity of the beds. The intensive current generated for the An/MS packed discharge suggests a higher degree of ionisation in a short time, thereby favoring chemical reactions [49]. We found that the discharge patterns were influenced by the electrical permittivities of different crystalline phases of TiO_2, and thus, correspondingly, affected the plasma chemistry of VOCs abatement.

One of the current questions regarding plasma-catalytic abatement of VOCs is related to the mechanisms of catalyst activation. Therefore, in order to understand the activation processes, we investigated the activation of photocatalysts in a plasma system. A comparison between UV light in the range of 250 – 400 nm from UV lamp and plasma discharge using the OES method was conducted to investigate the contribution of UV radiation to photocatalytic activity (Fig. 9). The lamp mainly emits light in the soft UV range at wavelengths of 365 nm and 313 nm. Meanwhile, most of the emissions from the discharge were formed due to the second positive system of the nitrogen molecule ($N_2 \, (C^3\Pi_u - B^3\Pi_g)$) [5]. The UV flux of the lamp integrated over the range 250 – 400 nm was estimated to be 2.7 mW/cm^2, whereas the flux generated in the discharge was 2.7 $\mu W/cm^2$ at an input power of 13.1 W, which is 10^3 orders lower than that of the UV lamp. Similar results with very low UV flux of plasma-generated photons caused low efficiency in the photocatalytic reactions, which is in agreement with previous research [26, 50]. This low flux is not sufficient for effective catalysts photo-activation and therefore, other mechanisms of photo-catalysts activation must occur in the DBD reactor. The number of adsorption sites on TiO_2 could also highly affect the generation of $O_2^{\bullet-}$, which is one of the key active oxidisers for VOCs abatement [1]. Using photo-dissociation, the UV flux of 1 $\mu W/cm^2$ can produce the chemiluminescence flux of $O_2^{\bullet-}$ 1×10^{14} cm^{-2} [51, 52]. Note that the flux of $O_2^{\bullet-}$ is sufficient for

photocatalyst activation by plasma-initiated photocatalytic reactions that assist with toluene oxidation.

In order to further investigate the effect of plasma-discharge on TiO_2 samples, the composition of the catalysts after discharge was analysed using XPS. Fig. S4 shows the simulated spectra of O 1s, and the atomic contents of O are summarised in Table 4. The formation of defects in TiO_2 was observed for all types of catalysts, which may be caused by the thermal effect of plasma discharge [43]. Vo accumulation accompanied the Ti^{3+} defects, and more oxidation radicals $O_2^{\bullet -}$ were expected to be created on the TiO_2 surface, assisting with toluene oxidation. However, the XRD results show that the crystalline phases were not affected in 90 min discharge (Fig. S5). Hence, the surface reactions were thought to be the main processes, and the discharge or electron impact may have little effect on the bulk structure of the catalysts.

For the photocatalysis activator, Whitehead et al. suggested that the electron created by the discharge impact upon the TiO_2 surface may stimulate electron–hole pair formation as UV photons did for further photocatalytic oxidation [53]. Another possible activation route that cannot be neglected is the variation of phase defects on the catalyst surface. The high energetic electron produced by surface discharging could be captured by Vo due to positive property of Vo, and then the adjacent VOCs, O_2, and N_2 could be activated to be $VOCs^{\bullet -}$, $O_2^{\bullet -}$, $N_2^{\bullet -}$, respectively, promoting the photocatalytic oxidation process [54]. Therefore, considering the mixed-phase catalysts in the plasma-photocatalytic process, three circumstances are illustrated in Fig. 10. Case i in Fig. 10 is a charge transfer process that occurs on the heterostructure-based P25 catalyst surface. Here, the excited electrons could migrate from the Ru to the conduction band of An, while holes accumulate in the valence band of Ru, leading to a reduction in electron–hole

recombination. This is thought to be beneficial to the photocatalysis process [55, 56]. Case ii represents the plasma-photocatalytic process of mechanically mixed TiO_2 sample (3An:1Ru) compared with P25. Herein, it appears that the charge transfer efficiency of 3An:1Ru is relatively low, exhibiting a lower synergistic effect [57]. This finding is also in agreement with the catalytic performances of 3An:1Ru. Finally, for the single-phase An and Ru samples (case iii), no charge transfer occurs on the surface of the An or Ru samples but it is suggested that the so-called synergetic effect might not promote all the photocatalytic oxidation processes [30]. In plasma system, it seems that for an An sample, the electrons created by discharge may be more efficiently utilised on the surface, resulting in further oxidation processes, and achieving the lowest unwanted byproducts (as seen in Fig. 6). A summary of the possible routes of the catalyst activation via the plasma-trigger reactions is shown in Fig. 10. Note that the plasma-trigger reactions include the possible activation process of photocatalytic oxidation in a plasma system (Processes 1-6 in Fig. 10), the transfer process of negative charge by the first steps of electron impact [58], and a series of follow-up reactions, such as the process of ionisation, dissociation, detachment, and excitation (processes 7-12 in Fig. 10).

The possible plasma-trigger reactions in Fig. 10 are as follows:

TiO_2 + energy (hv, electron impacts) $\rightarrow h^+ + e^-$ $O_2 + e^- \rightarrow O_2^{\bullet-}$ $h^+ + Sur\text{-}OH^- \rightarrow OH^\bullet$	Process (1-3) in Fig. 10
$TiO_2 (Vo) + e^-$ (surface discharge) $\rightarrow TiO_2 (Vo)^-$ Adjacent VOCs , N_2, $O_2 + TiO_2 (Vo)^- \rightarrow VOCs^{\bullet-}, O_2^{\bullet-}, N_2^{\bullet-} + TiO_2 (Vo)$	Process (5-6) in Fig. 10
$N_2 + e \rightarrow N_2^+ + 2e$	Process (7-8) in Fig. 10

$N_2 + e \rightarrow N_2\,(A^3\Sigma, B^3\Pi, C^3\Pi)$	
$N_2\,(A^3\Sigma) + O_2 \rightarrow N_2\,(X^1\Sigma) + O + O$	Process (9) in Fig. 10
$N_2\,(B^3\Sigma) + O_2 \rightarrow N_2\,(X^1\Sigma) + O + O$	
$O + O_2 + O_2 \rightarrow O_3 + O_2$	Process (10-11) in Fig. 10
$O + O_2 + N_2 \rightarrow O_3 + N_2$	
$O_3 + h\nu \rightarrow O^{\bullet} + O_2$	
$O_2 + e \rightarrow O + O^-$	
$C_6H_5CH_3 + e \rightarrow C_6H_5CH_2\bullet + \bullet H$	Process (12) in Fig. 10
$C_6H_5CH_3 + e \rightarrow C_6H_5\bullet + \bullet CH_3$	

3.4. The analysis of toluene degradation pathways

It is believed that side reaction products from Fig. 6 are only gaseous byproducts as no obvious poly-aromatic organic compounds were observed on the surface of catalysts after toluene treatment as seen in Fig. S6. This was further confirmed by the results of the TG-MS (Fig. S7). The first step of weight loss at temperatures up to 200°C was attributed to the elimination of physisorbed and chemisorbed water [59]. This weight loss slowed down until the temperature was higher than 650°C. Note that there were no detected compounds reported in the TG-MS. The poly-aromatic organic compounds produced during plasma discharge were involved in the reaction of ozone and hydroxyl radicals [60]. Considering the suppression of ozone in our discharge system (Fig. S8), a solid byproduct was believed to be suppressed as well. Meanwhile, the long-term air discharge (90 min) also helped "self-clean" the process, further removing surface byproducts [61].

The observed consumption of ozone (Fig. S8), was attributed to its self-decomposition and involvement in the reactions of NOx generation. The strong emission of the nitrogen second

positive system (0−0 vibrational band of N_2 ($C^3\Pi_u - B^3\Pi g$)) was used to determine the N_2 rotational temperature and the results of the spectral analysis are summarised in Table 3. The relatively high N_2 rotational temperature, which corresponds to the central part of the microdischarges, results in the decomposition of ozone [5]. The temperature of the DBD reactor wall was measured to be ~373 k, also implying a possible thermal effect on O_3 decomposition (process 10 in Fig. 10). Simultaneously, as seen in Fig. 11a, the high concentration of NOx (NO and NO_2) also caused a discharge poisoning effect, leading to the ozone inhibition [62]. Note that in Fig. 11b, NO concentration gradually increased as a function of time, and in the photocatalysis system, its concentration was much higher than that in the plasma-MS system. Further, the highest NOx (NO and NO_2) concentration was generated in the presence of An/MS. It was easy to oxidise NO into NO_2 in the presence of ozone, which leads to a higher NO_2 concentration. Note that, herein, the opposite result was observed, implying that ozone may be consumed before participating in the reaction of NO_2 generation [50]. Ozone can act as an acceptor of an electron created by discharge ($O_3 + e^- \rightarrow O_3^- \rightarrow O^{\bullet-} + O_2$) [23], and the reaction rate of toluene and atomic O ($k = 7.6 \times 10^{-14}$ molecule cm^{-3} s^{-1}) is faster than the reaction of toluene oxidation with ozone ($k = 3.9 \times 10^{-22}$ molecule cm^{-3} s^{-1}) [63], which might imply that atomic O was involved in toluene oxidation. The vibrationally excited nitrogen molecules (N_2*(vib)) produced by discharge follow endothermic and exothermic steps to form NO ($O + N_2$*(vib) $\rightarrow$ NO + N, N $+ O_2 \rightarrow$ NO + N) [11]. The relative intensity of the nitrogen vibrational bands in the OES spectra was recorded (Fig. 12), and we found that with a higher intensity of N_2*(vib), a higher NOx generation was achieved, suggesting that the diversity of N_2*(vib) generation in the presence of different samples was related to the discrepancy of NOx generation.

It is difficult to draw conclusions on the effects of titanium oxide crystalline phase on gaseous organic byproducts when different amounts of toluene are adsorbed. However, the promotion of fewer byproducts as a result of plasma-photocatalysis can be observed (Fig. 13). These byproducts include 1,3-Butadiyne (C_4H_2), guanidine, methyl- ($C_2H_7N_3$), and were only found in the plasma-MS system, which suggests this system used a different toluene degradation pathway. Hence, the reactive plasma species in the plasma-MS system was believed to be the reason toluene degradation formed these byproducts. With the assistance of photocatalytic reactions, it was believed that C_4H_2 and $C_2H_7N_3$ were further oxidised into small molecular byproducts or CO_X, which can be confirmed by the improved carbon balance (Fig. 6). The pathway of toluene decomposition in the plasma-photocatalytic system is proposed as shown in Fig.14. Note that other byproducts can be sorted into three types: Benzenoids, Nitrogenous organic compound, and Oxy-organics (Table S2). Benzenoids were revealed in the plasma-AgMn/SBA-15 system [4], plasma-Co/MCM-15 system [63], plasma alone [64], and in our plasma system with/without photocatalysts, suggesting these ring-retaining products may be first toluene-decomposition steps caused by the primarily reactive plasma species (Eqs. 1.1-1.4 in Table 5). Meanwhile, note that photocatalytic reactions could also contribute to form benzenoids (Eqs. 2.1-2.5 in Table 5). Owing to the adsorption-discharge process, most oxidation reactions were believed to occur on/around the catalyst surface [65]. Then, the highly energetic electron, mainly from the surface discharge, stimulated a series of reactive plasma species generation and activated photocatalytic reactions, promoting ring-opening. Subsequently, electron collision was thought to be the first step for toluene oxidation ($C_6H_5CH_3 + e^- \rightarrow$ products, $k = 10^{-6}$ cm^3 molecule^{-1} s^{-1}) [48, 66]. The mean electron energy of 4.7 eV in the plasma-P25 discharge aided toluene removal when the removal of

H from methyl only required ~3.9 eV [67], which could help explain the carbon balance with the lowest remaining toluene. Acetone was found to be a typical byproduct in the plasma-photocatalysis system [1, 68], which is generated with the assistance of $O^{\bullet -}$ and, $O_2^{\bullet -}$ produced during the photocatalytic process (Eqs. 2.1-2.2 in Table 5) [1, 10], and the discharge (Eqs. 1.5-1.7 in Table 5) [62]. Other byproducts exhibited characteristics of lower carbon composition, which reflects a higher CO_X yield.

The GC-MS spectra in the plasma-An/MS system was also studied as a function of discharging time (Fig. 13B). The yield of the byproducts was maximum at the beginning of discharge (at 90 s). After this, most byproducts such as benzenoids (except for toluene), methyl nitrite (CH_3NO_2), acetonitrile (C_2H_3N), acetone (C_3H_6O), methyl nitrate (CH_3NO_3), and acetic acid ethenyl-($C_4H_6O_2$), decreased sharply with the increase in reaction time. Note that, the intensities of these byproducts were lower than the detection limit after 30 min of discharge. The concentration of NOx increased at 30 min, as shown in Fig. 11a, implying the possible degradation pathway of methyl nitrite, acetonitrile and methyl nitrate to NOx. In addition, note that the intensity of ethylamine (C_2H_7N) and acetaldehyde (C_2H_4O) were not affected by discharging time, which suggests that they are possible "transit" byproducts with similar generation and decomposition rates.

3.5. Stability performance of An/MS catalyst

A stability test involving seven continuous adsorption-discharging cycles with An/MS was performed (Fig. 15). The results showed that CO_2 yield slowly decreased from ~70% to ~63% in

the first stages, exhibiting a partial deactivation before reaching a quasi-stationary state. A slight decrease (approximately 6%) of the adsorption capacity was also observed. The physicochemical properties of the used An/MS were characterised. As seen in Fig. 16, no significant change was observed in the XRD patterns after the stability test, indicating that the crystalline phase of An was not affected by plasma discharge. Meanwhile, there were no obvious surface morphology changes of An/MS found before and after stability testing (Fig. S9), which indicates that there were less carbonaceous deposits on the catalyst surface after the stability tests. However, note that there was a remarkable change of XPS spectra, as seen in Fig. S10, revealing that more O-Ti^{4+} formed, which indicates that the sample was oxidised by plasma discharge and/or thermal effects. Meanwhile, the O vacancy of the An/MS sample was found to decrease after the stability test, suggesting the possible irreversible change in the crystalline structure was ongoing.

Conclusions

In this study, the influence of the different crystalline phases of TiO_2 incorporated in a MS were used as photocatalysts, and the plasma- photocatalytic degradation of toluene was investigated. Herein, we have determined the following conclusions:

(i)   The photocatalytic reactions were affected by the physicochemical properties of the mixed phase TiO_2. The UV absorption ability of catalysts and the dispersion of the adsorption site (Vo) played important roles in photocatalytic performance.

(ii)   Regarding the carbon balance results, the An sample had the highest CO_X yield. However, the high relative permittivity of P25 led to an enhancement of the electrical field and more intensive plasma, resulting in the highest total toluene conversion.

(iii)   We found that the surface reactions on catalysts were of key importance in toluene abatement initiated during in the adsorption-plasma catalytic process. Direct activation of the catalysts by UV photons originating from the discharge proved to play a minor role in DBD as a result of the very low intensity of the UV flux. More efforts should be put on in-site investigation of O radicals.

(iv)   We found no obvious effects of TiO_2 crystalline phases on the generation of organic byproducts generation. Most gaseous organic byproducts were degraded whitin 30 min of the discharging time, with the exception of ethylamine and acetaldehyde. The poly-aromatic organic compounds and ozone were suppressed while the NOx concentration accumulated.

Acknowledgments

References:

[1] H. Ye, Y. Liu, S. Chen, H. Wang, Z. Liu, Z. Wu, Synergetic effect between non-thermal plasma and photocatalytic oxidation on the degradation of gas-phase toluene: Role of ozone, Chinese. J. Catal. 40 (2019) 631-637.

[2] Z. Ye, J.M. Giraudon, N. Nuns, P. Simon, N. De Geyter, R. Morent, J.F. Lamonier, Influence of the preparation method on the activity of copper-manganese oxides for toluene total oxidation, Appl. Catal. B: Environ. 223 (2018) 154-166.

[3] X. Pan, M.Q. Yang, X. Fu, N. Zhang, Y.J. Xu, Defective TiO_2 with oxygen vacancies: synthesis, properties and photocatalytic applications, Nanoscale. 5 (2013) 3601-3614.

[4] X. Xu, P. Wang, W. Xu, J. Wu, L. Chen, M. Fu, D. Ye, Plasma-catalysis of metal loaded SBA-15 for toluene removal: Comparison of continuously introduced and adsorption-discharge plasma system, Chem. Eng. J. 283 (2016) 276-284.

[5] Z. Ye, S.K.P. Veerapandian, I. Onyshchenko, A. Nikiforov, N. De Geyter, J.-M. Giraudon, J.-F. Lamonier, R. Morent, An in-depth investigation of toluene decomposition with a glass beads-packed bed dielectric barrier discharge reactor, Ind. Eng. Chem. Res. 56 (2017) 10215-10226.

[6] H. Song, F. Hu, Y. Peng, K. Li, S. Bai, J. Li, Non-thermal plasma catalysis for chlorobenzene removal over $CoMn/TiO_2$ and $CeMn/TiO_2$: Synergistic effect of chemical catalysis and dielectric constant, Chem. Eng. J. 347 (2018) 447-454.

[7] X. Yao, J. Zhang, X. Liang, C. Long, Plasma-catalytic removal of toluene over the supported manganese oxides in DBD reactor: Effect of the structure of zeolites support, Chemosphere. 208 (2018) 922-930.

[8] T. Butterworth, R.W.K. Allen, Plasma-catalyst interaction studied in a single pellet DBD reactor: dielectric constant effect on plasma dynamics. Plasma Sources Sci. Technol. 19 (2017) 065008.

[9] F. Holzer, F.D. Kopinke, U. Roland, Influence of ferroelectric materials and catalysts on the performance of non-thermal plasma (NTP) for the removal of air pollutants, Plasma Chem. Plasma Process. 25 (2005) 595-611.

[10] H. Wang, S. Chen, Z. Wang, Y. Zhou, Z. Wu, A novel hybrid Bi_2MoO_6-MnO_2 catalysts with the superior plasma induced pseudo photocatalytic-catalytic performance for ethyl acetate degradation, Appl. Catal. B: Environ. 254 (2019) 339-350.

[11] X. Tang, J. Wang, H. Yi, S. Zhao, N_2O formation characteristics in dielectric barrier discharge reactor for environmental application: Effect of operating parameters, Energy Fuels. 31 (2017) 13901-13908.

[12] T. Zadi, A.A. Assadi, N. Nasrallah, R. Bouallouche, P.N. Tri, A. Bouzaza, M.M. Azizi, R. Maachi, D. Wolbert, Treatment of hospital indoor air by a hybrid system of combined plasma with photocatalysis: Case of trichloromethane, Chem. Eng. J. 349 (2018) 276-286.

[13] A.A. Assadi, S. Loganathan, P.N. Tri, S. Gharib-Abou Ghaida, A. Bouzaza, A.N. Tuan, D. Wolbert, Pilot scale degradation of mono and multi volatile organic compounds by surface discharge plasma/TiO_2 reactor: Investigation of competition and synergism, J. Hazard. Mater. 357 (2018) 305-313.

[14] G. Maxime, A.A. Amine, B. Abdelkrim, W. Dominique, Removal of gas-phase ammonia and hydrogen sulfide using photocatalysis, nonthermal plasma, and combined plasma and photocatalysis at pilot scale, Environ. Sci. Pollut. Res. 21 (2014) 13127-13137.

[15] S. Gharib-Abou Ghaida, A.A. Assadi, G. Costa, A. Bouzaza, D. Wolbert, Association of surface dielectric barrier discharge and photocatalysis in continuous reactor at pilot scale: Butyraldehyde oxidation, by-products identification and ozone valorization, Chem. Eng. J. 292 (2016) 276-283.

[16] J. Hu, N. Jiang, J. Li, K. Shang, N. Lu, Y. Wu, Degradation of benzene by bipolar pulsed series surface/packed-bed discharge reactor over MnO_2 - TiO_2 /zeolite catalyst, Chem. Eng. J. 293 (2016) 216-224.

[17] B.Y. Lin, M.B. Chang, H.L. Chen, H.M. Lee, S.J. Yu, S.N. Li, Removal of C_3F_8 via the combination of non-thermal plasma, adsorption and catalysis, Plasma Chem. Plasma Process. 31 (2011) 585-594.

[18] W.A. Saoud, A.A. Assadi, M. Guiza, S. Loganathan, A. Bouzaza, W. Aboussaoud, A. Ouederni, S. Rtimi, D. Wolbert, Synergism between non-thermal plasma and photocatalysis: Implicationsin the post discharge of ozone at a pilot scale in a catalytic fixed-bed reactor, Appl. Catal. B: Environ. 241 (2019) 227-235.

[19] Z. Ye, C. Wang, Z. Shao, Q. Ye, Y. He, Y. Shi, A novel dielectric barrier discharge reactor with photocatalytic electrode based on sintered metal fibers for abatement of xylene, J. Hazard. Mater. 241-242 (2012) 216-223.

[20] H. Guo, N. Jiang, H. Wang, K. Shang, N. Lu, J. Li, Y. Wu, Enhanced catalytic performance of graphene-TiO_2 nanocomposites for synergetic degradation of fluoroquinolone antibiotic in pulsed discharge plasma system, Appl. Catal. B: Environ. 248 (2019) 552-566.

[21] H.-H. Kim, S.-M. Oh, A. Ogata, S. Futamura, Decomposition of gas-phase benzene using plasma-driven catalyst (PDC) reactor packed with Ag/TiO_2 catalyst, Appl. Catal. B: Environ. 56 (2005) 213-220.

[22] A. Maciuca, C. Batiot-Dupeyrat, J.-M. Tatibouët, Synergetic effect by coupling photocatalysis with plasma for low VOCs concentration removal from air, Appl. Catal. B: Environ. 125 (2012) 432-438.

[23] I. Aouadi, J.M. Tatibouët, L. Bergaoui, MnO_X/TiO_2 catalysts for VOCs abatement by coupling non-thermal plasma and photocatalysis, Plasma Chem. Plasma Process. 36 (2016) 1485-1499.

[24] J. Van Durme, J. Dewulf, K. Demeestere, C. Leys, H. Van Langenhove, Post-plasma catalytic technology for the removal of toluene from indoor air: Effect of humidity, Appl. Catal. B: Environ. 87 (2009) 78-83.

[25] E. Acayanka, D.S. kuete, G.Y. Kamgang, S. Nzali, S. Laminsi, P.T. Ndifon, Synthesis, characterization and photocatalytic application of TiO_2/SnO_2 nanocomposite obtained under non-thermal plasma condition at atmospheric pressure, Plasma Chem. Plasma Process. 36 (2016) 799-811.

[26] T. Sano, N. Negishi, E. Sakai, S. Matsuzawa, Contributions of photocatalytic/catalytic activities of TiO_2 and γ-Al_2O_3 in nonthermal plasma on oxidation of acetaldehyde and CO, J. Mol. Catal. A: Chem. 245 (2006) 235-241.

[27] H.B. Huang, D.Q. Ye, M.L. Fu, F.D. Feng, Contribution of UV light to the decomposition of toluene in dielectric barrier discharge plasma/photocatalysis system, Plasma Chem. Plasma Process. 27 (2007) 577-588.

[28] L. Shen, Z. Xing, J. Zou, Z. Li, X. Wu, Y. Zhang, Q. Zhu, S. Yang, W. Zhou, Black TiO_2 nanobelts/g-C_3N_4 nanosheets Laminated Heterojunctions with Efficient Visible-Light-Driven Photocatalytic Performance, Sci Rep. 7 (2017) 41978.

[29] X. Xin, T. Xu, J. Yin, L. Wang, C. Wang, Management on the location and concentration of Ti^{3+} in anatase TiO_2 for defects-induced visible-light photocatalysis, Appl. Catal. B: Environ. 176-177 (2015) 354-362.

[30] P. Apopei, C. Catrinescu, C. Teodosiu, S. Royer, Mixed-phase TiO_2 photocatalysts: Crystalline phase isolation and reconstruction, characterization and photocatalytic activity in the oxidation of 4-chlorophenol from aqueous effluents, Appl. Catal. B: Environ. 160-161 (2014) 374-382.

[31] D.M. Tobaldi, R.C. Pullar, M.P. Seabra, J.A. Labrincha, Fully quantitative X-ray characterization of Evonik Aeroxide TiO_2 P25®, Materials Letters. 122 (2014) 345-347.

[32] Z. Chen, H.N. Dinh, E. Miller, Photoelectrochemical water splitting (pp. 57-60). New York: Springer, 2013.

[33] E. Stoffels, A.J. Flikweert, W.W. Stoffels, G.M.W. Kroesen, Plasma needle: a non-destructive atmospheric plasma source for fine surface treatment of (bio) materials, Plasma Sources Sci. Technol. 11 (2002) 383-388.

[34] C.O. Laux, T.G. Spence, C.H. Kruger, R.N. Zare, Optical diagnostics of atmospheric pressure air plasmas, Plasma Sources Sci. Technol. 12 (2003) 125-138.

[35] C.O. Laux, 2002. Radiation and nonequilibrium collisional-radiative models, von karman institute for fluid dynamics, Lecture Series 2002–7, Rhode Saint-Genese, Belgium.

[36] H. Nassar, S. Pellerin, K. Musiol, O. Martinie, N. Pellerin, J.M. Cormier, N_2^+/N_2 ratio and temperature measurements based on the first negative N_2^+ and second positive N_2 overlapped molecular emission spectra, J. Phys. D: Appl. Phys. 37 (2004) 1904-1916.

[37] P. Paris, M. Aints, F. Valk, T. Plank, A. Haljaste, K.V. Kozlov, H.E. Wagner, Reply to comments on 'Intensity ratio of spectral bands of nitrogen as a measure of electric field strength in plasmas', J. Phys. D: Appl. Phys. 39 (2006) 2636-2639.

[38] P. Paris, M. Aints, M. Laan, F. Valk, Measurement of intensity ratio of nitrogen bands as a function of field strength, J. Phys. D: Appl. Phys. 37 (2004) 1179-1184.

[39] K.V. Kozlov, H.-E. Wagner, R. Brandenburg, P. Michel, Spatio-temporally resolved spectroscopic diagnostics of the barrier discharge in air at atmospheric pressure, J. Phys. D: Appl. Phys. 34 (2001) 3164-3176.

[40] P. Paris, M. Aints, F. Valk, T. Plank, A. Haljaste, K.V. Kozlov, H.E. Wagner, Intensity ratio of spectral bands of nitrogen as a measure of electric field strength in plasmas, J. Phys. D: Appl. Phys. 38 (2005) 3894-3899.

[41] J. Gong, A. Imbault, R. Farnood, The promoting role of bismuth for the enhanced photocatalytic oxidation of lignin on Pt-TiO_2 under solar light illumination, Appl. Catal. B: Environ. 204 (2017) 296-303.

[42] L. Pan, T. Muhammad, L. Ma, Z.-F. Huang, S. Wang, L. Wang, J.-J. Zou, X. Zhang, MOF-derived C-doped ZnO prepared via a two-step calcination for efficient photocatalysis, Appl. Catal. B: Environ. 189 (2016) 181-191.

[43] X. Kong, Y. Xu, Z. Cui, Z. Li, Y. Liang, Z. Gao, S. Zhu, X. Yang, Defect enhances photocatalytic activity of ultrathin TiO_2 (B) nanosheets for hydrogen production by plasma engraving method, Appl. Catal. B: Environ. 230 (2018) 11-17.

[44] K.L. Schulte, P.A. DeSario, K.A. Gray, Effect of crystal phase composition on the reductive and oxidative abilities of TiO_2 nanotubes under UV and visible light, Appl. Catal. B: Environ. 97 (2010) 354–360.

[45] N.S. Allen, N. Mahdjoub, V. Vishnyakov, P.J. Kelly, The effect of crystalline phase (anatase, brookite and rutile) and size on the photocatalytic activity of calcined polymorphic titanium dioxide (TiO_2), Polym. Degrad. Stabil. 150 (2018) 31–36.

[46] J. Zhang, P. Zhou, J. Liu, J. Yu, New understanding of the difference of photocatalytic activity among anatase, rutile and brookite TiO_2. Phys. Chem. Chem. Phys. 16 (2014) 20382-20386.

[47] J.C. Whitehead, Plasma–catalysis: the known knowns, the known unknowns and the unknown unknowns, J. Phys. D: Appl. Phys. 49 (2016) 243001.

[48] A.U. Rehman, S.F. Shaukat, M.N. Akhtar, M. Ahmad, Evaluations of structural, magnetic and various dielectric parameters of Nisubstituted Zn_2W-type hexagonal ferrites for high frequency (1–6 GHz) applications, Ceram. Int. 45 (2019) 24202–24211

[49] H.-H. Kim, Y. Teramoto, N. Negishi, A. Ogata, A multidisciplinary approach to understand the interactions of nonthermal plasma and catalyst: A review, Catal. Today. 256 (2015) 13-22.

[50] H.H. Kim, A. Ogata, Nonthermal plasma activates catalyst: from current understanding and future prospects, Eur. Phys. J. Appl. Phys. 55 (2011) 13806.

[51] K.-i. Ishibashi, A. Fujishima, T. Watanabe, K. Hashimoto, Generation and deactivation processes of superoxide formed on TiO_2 film illuminated by very weak UV light in air or water, J. Phys. Chem. B. 104 (2000) 4934-4938.

[52] K.-i. Ishibashi, Y. Nosaka, K. Hashimoto, A. Fujishima, Time-dependent behavior of active oxygen species formed on photoirradiated TiO$_2$ films in air, J. Phys. Chem. B. 102 (1998) 2117-2120.

[53] J.C. Whitehead, Plasma catalysis: A solution for environmental problems, Pure Appl. Chem. 82 (2010) 1329-1336.

[54] I. Nakamura, N. Negishi, S. Kutsuna, T. Ihara, S. Sugihara, K. Takeuchi, Role of oxygen vacancy in the plasma-treated TiO$_2$ photocatalyst with visible light activity for NO removal, J. Mol. Catal. A: Chem. 161 (2000) 205-212.

[55] T. Ohno, K. Sarukawa, K. Tokieda, M. Matsumura, Morphology of a TiO$_2$ Photocatalyst (Degussa, P-25) Consisting of Anatase and Rutile Crystalline Phases, J. Catal. 203 (2001) 82-86.

[56] D.C. Hurum, A.G. Agrios, K.A. Gray, T. Rajh, M.C. Thurnauer, Explaining the enhanced photocatalytic activity of Degussa P25 mixed-phase TiO$_2$ using EPR, J. Phys. Chem. B.107 (2003) 4545-4549.

[57] X.L. Wang, S. Shen, Z.C. Feng, C. Li, Time-resolved photoluminescence of anatase/rutile TiO2 phase junction revealing charge separation dynamics. Chinese. J. Catal. 37 (2016) 2059-2068.

[58] T. Zhu, et al., VOCs decomposition via modified ferroelectric packed bed dielectric barrier discharge plasma. IEEE Trans. Plasma. Sci. 39 (2011) 1695-1700.

[59] S. Sultana, Z. Ye, S.K.P. Veerapandian, A. Löfberg, N. De Geyter, R. Morent, J.-M. Giraudon, J.-F. Lamonier, Synthesis and catalytic performances of K-OMS-2, Fe/K-OMS-2 and Fe-K-OMS-2 in post plasma-catalysis for dilute TCE abatement, Catal. Today. 307 (2018) 20-28.

[60] F.M. Bowman, C. Pilinis, J.H. Seinfeld, Ozone and aerosol productivity of reactive organics, Atmos. Environ. 29 (1995) 579-589.

[61] J. Van Durme, J. Dewulf, C. Leys, H. Van Langenhove, Combining non-thermal plasma with heterogeneous catalysis in waste gas treatment: A review, Appl. Catal. B: Environ. 78 (2008) 324–333.

[62] X.L. Deng, A.Y. Nikiforov, P. Vanraes, Direct current plasma jet at atmospheric pressure operating in nitrogen and air, J. Appl. Phys. 113 (2013) 023305.

[63] X. Xu, J. Wu, W. Xu, M. He, M. Fu, L. Chen, A. Zhu, D. Ye, High-efficiency non-thermal plasma-catalysis of cobalt incorporated mesoporous MCM-41 for toluene removal, Catal. Today. 281 (2017) 527-533.

[64] A.M. Vandenbroucke, R. Morent, N.D. Geyter, C. Leys, Decomposition of toluene with plasma-catalysis: A review, J. Adv. Oxid. Technol. 15 (2012) 232-241.

[65] E.C. Neyts, K.K. Ostrikov, M.K. Sunkara, A. Bogaerts, Plasma catalysis: Synergistic effects at the nanoscale, Chem. Rev. 115 (2015) 13408-13446.

[66] H. Kohno, A.A. Berezin, J.-S. Chang, Destruction of volatile organic compounds used in a semiconductor industry by a capillary tube discharge reactor, IEEE T. Dielect. El. In. 34 (1998) 953-966.

[67] K. Urashima, J.-S. Chang, Removal of volatile organic compounds from air streams and industrial flue gases by non-thermal plasma technology, IEEE T. Dielect. El. In. 7 (2000) 602-614.

[68] A.A. Assadi, A. Bouzaza, C. Vallet, D. Wolbert, Use of DBD plasma, photocatalysis, and combined DBD plasma/photocatalysis in a continuous annular reactor for isovaleraldehyde elimination – Synergetic effect and byproducts identification, Chem. Eng. J. 254 (2014) 124-132.
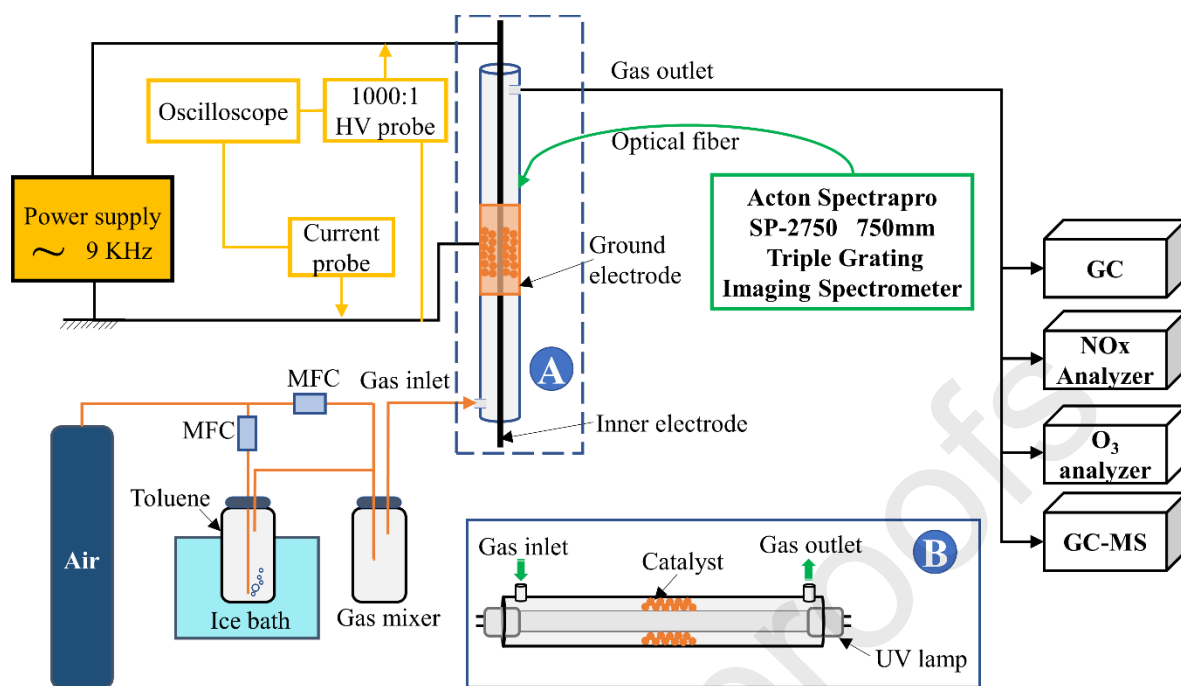
Fig. 1. The schematic diagram of the experimental set-up.
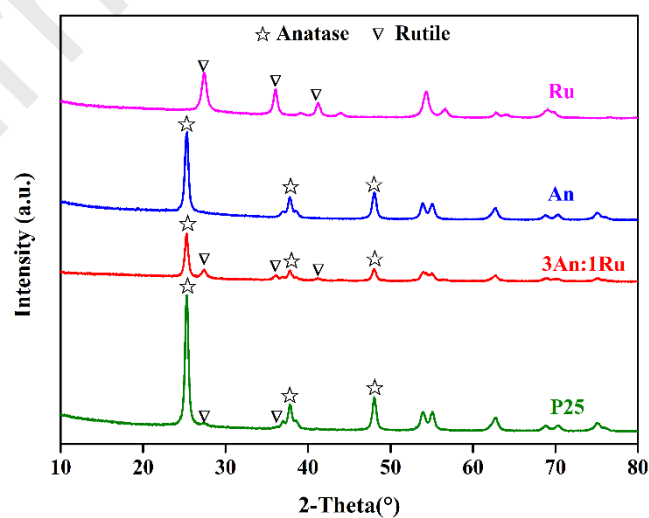
Fig. 2. XRD patterns of TiO$_2$ samples.
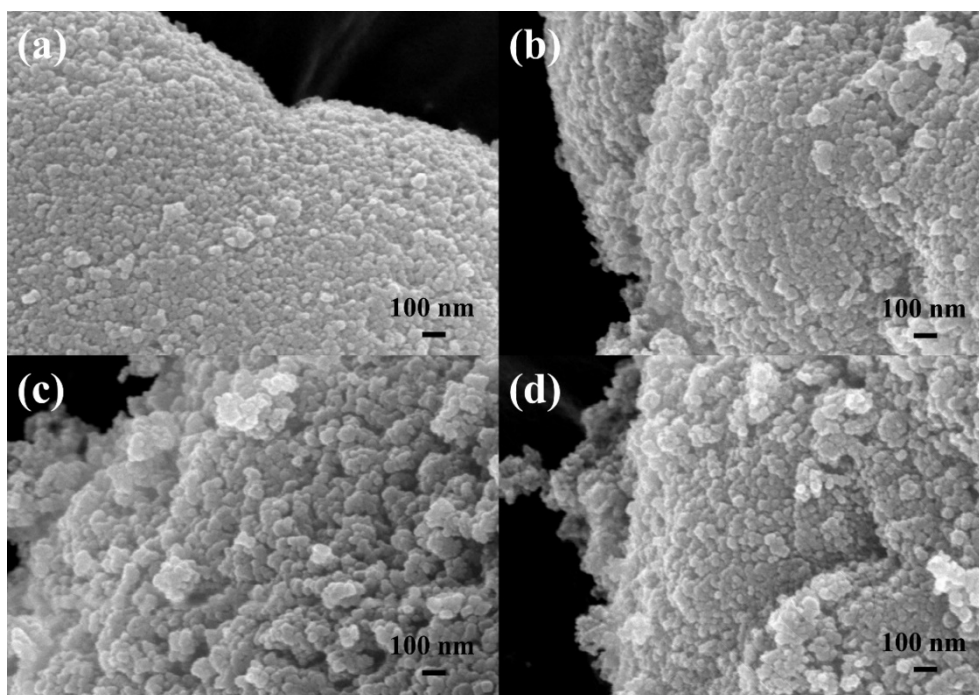
Fig. 3. SEM images of (a) An, (b) Ru, (c) P25 and (d) 3An:1Ru catalysts.
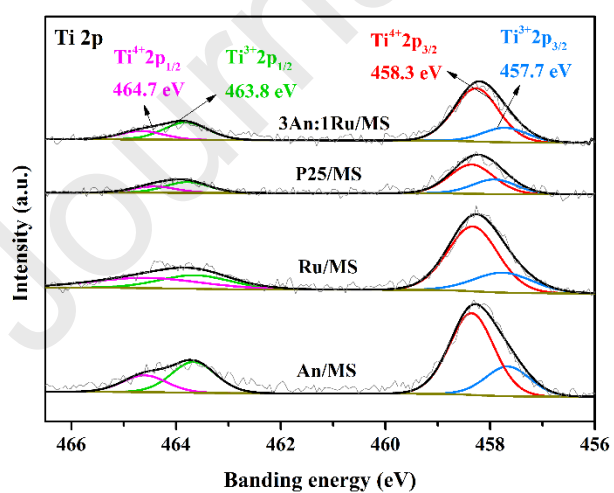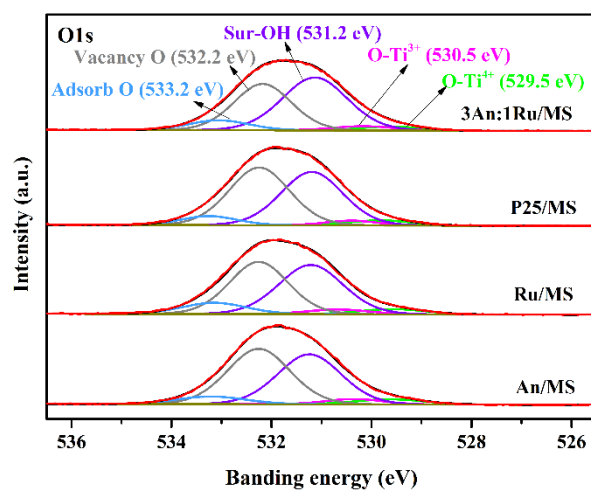
Fig. 4. XPS spectra of Ti 2p peaks and O 1s peaks for titanium samples.
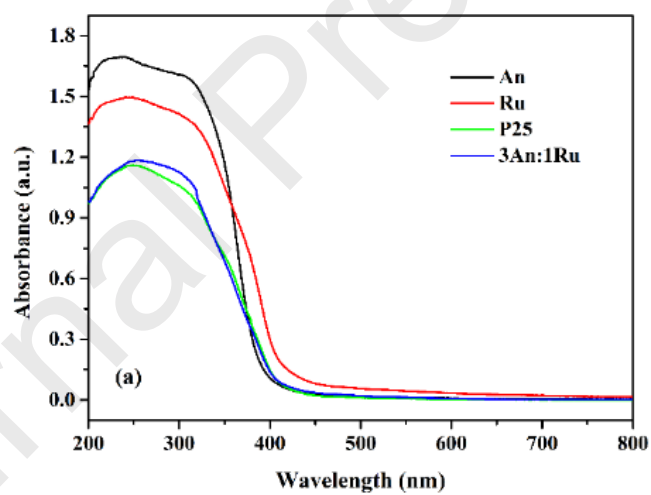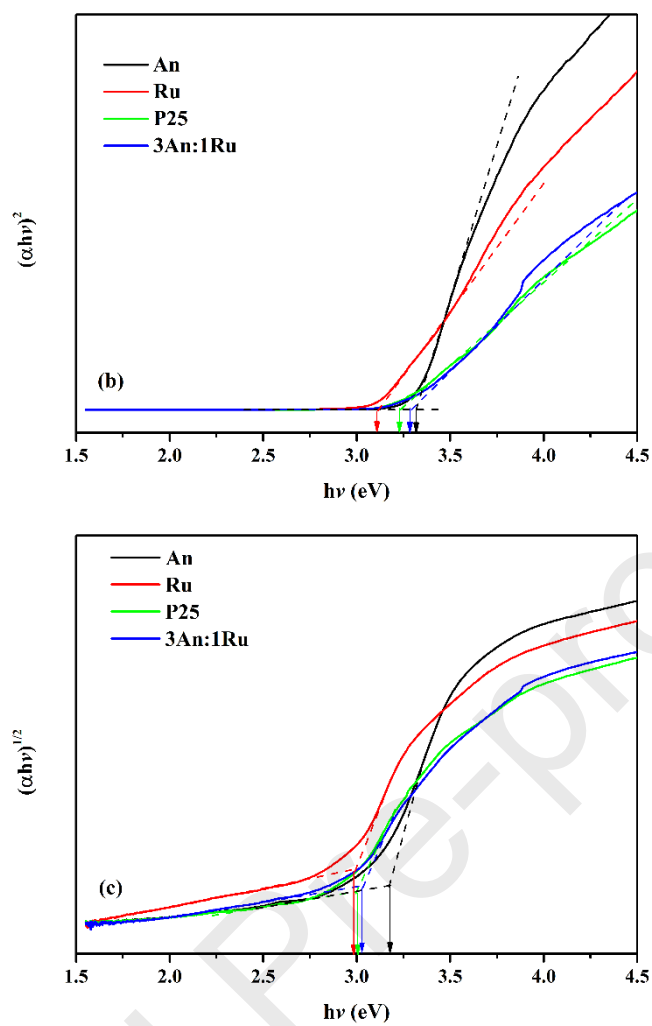
Fig. 5. (a) UV-vis absorbance spectra, (b) optical direct and (c) indirect band-gap of different catalysts.
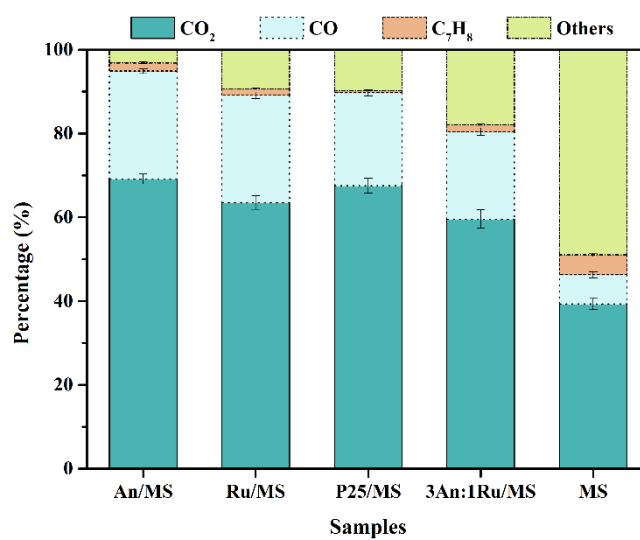
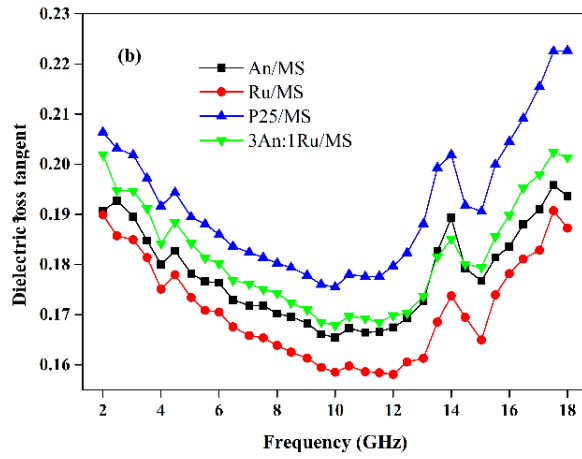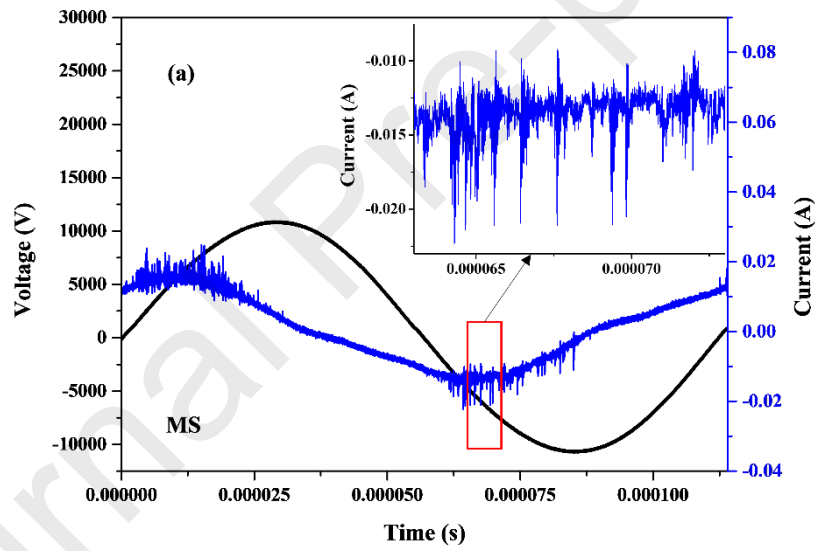Fig.6. Carbon balances of a gas phase after DBD reactor treatment for different catalyst samples.
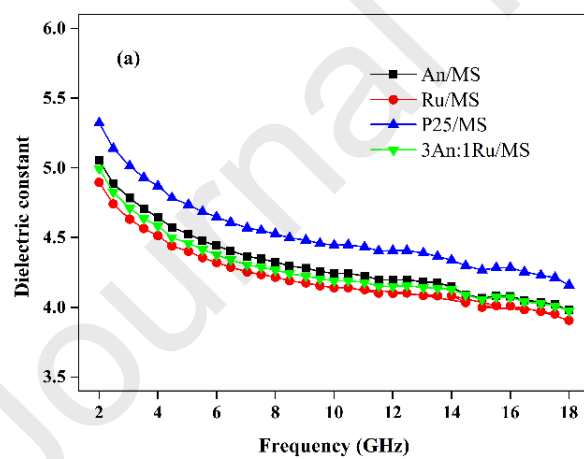
Fig. 7. Variation of dielectric constant (a) and dielectric loss tangent (b) of titanium samples with frequency.
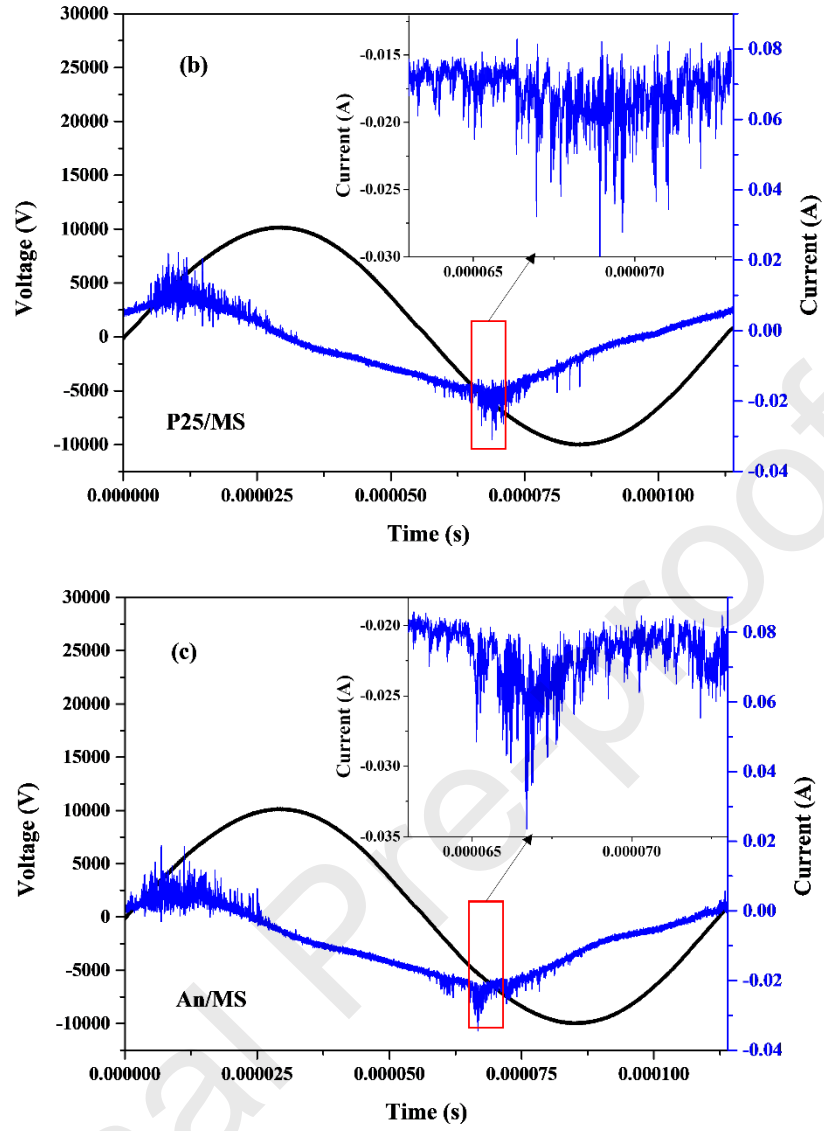
Fig. 8. Typical voltage-current waveforms at the input power of 13.1 W (frequency: 9 kHz; (a) MS, (b) P25/MS, and (c) An/MS).
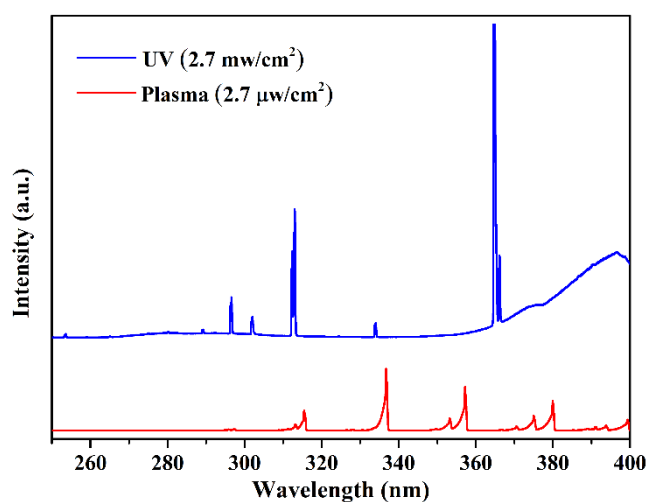
Fig. 9. Spectral characteristics of the UV radiation in the range of 250-400 nm in DBD-Plasma system and UV system with indication of the total UV flux in the range 250-400 nm.
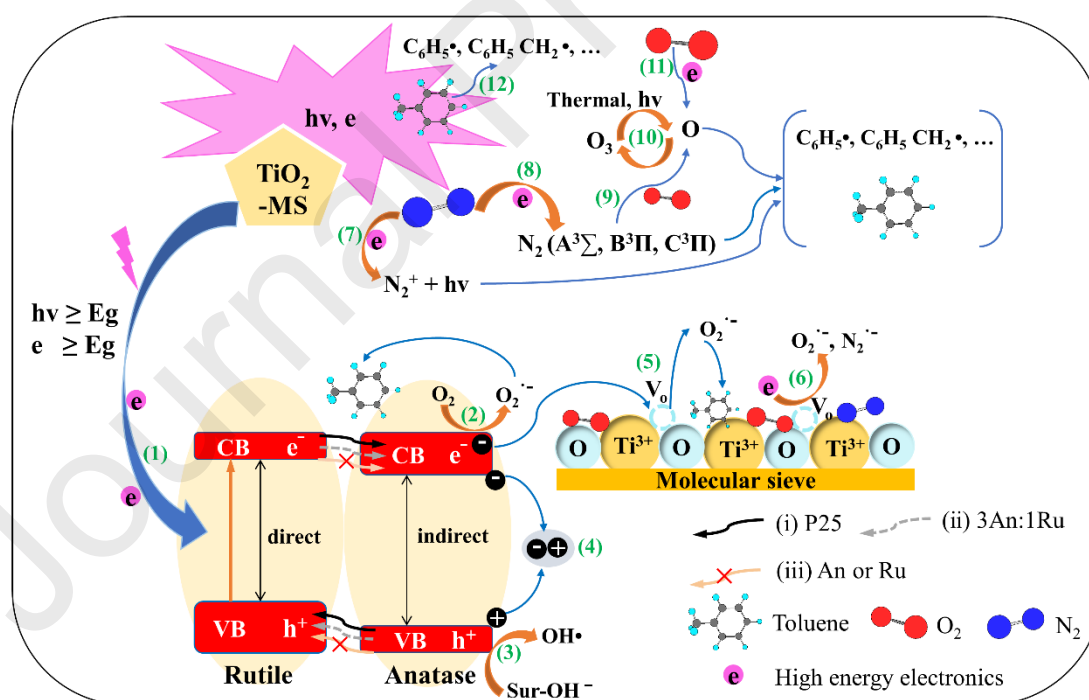
Fig. 10. The synergetic mechanisms of toluene degradation in plasma-photocatalysis process.
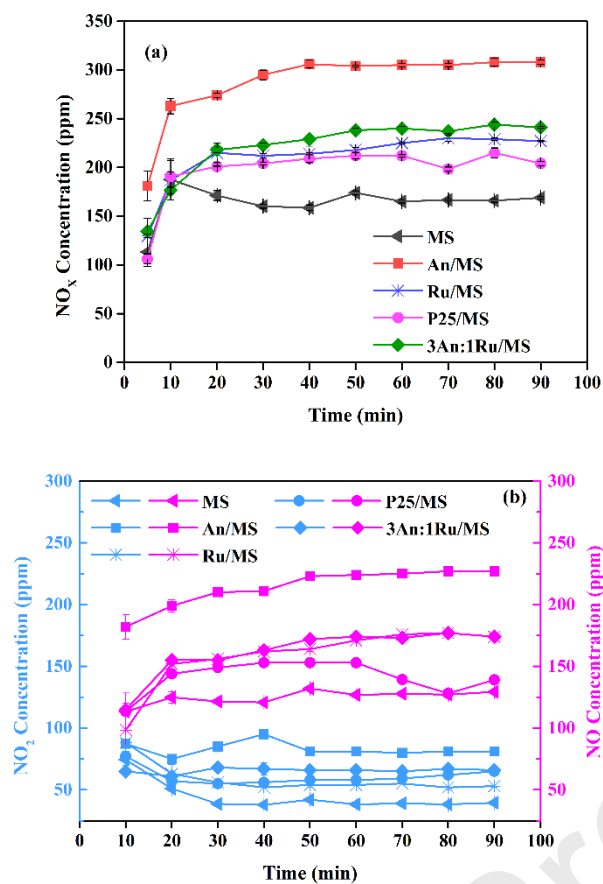
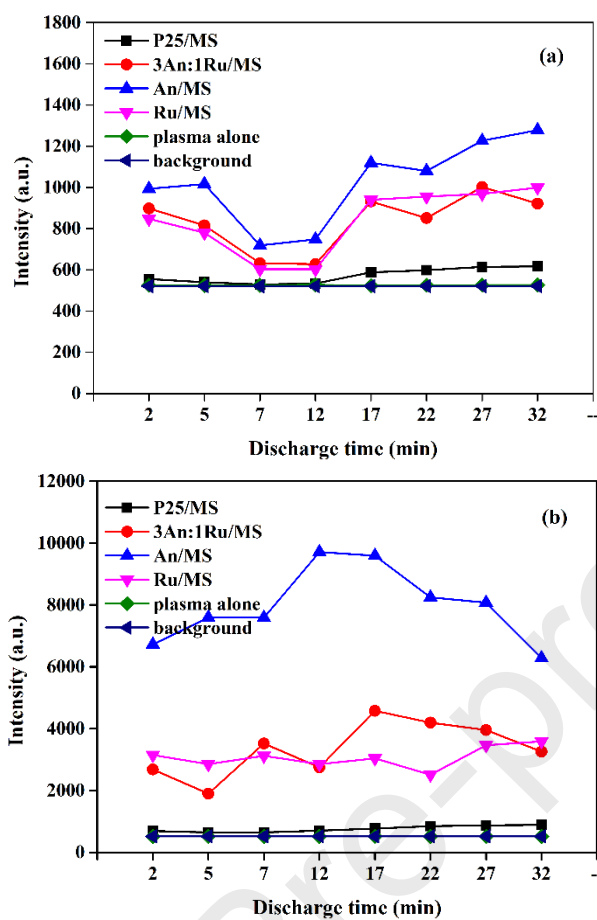Fig. 11. Concentration of (a) NO_X, (b) NO and NO_2 on various catalysts at different discharge time.

Fig. 12. Measured (a) N_2^+ B–X spectrum and (b) N_2 C–B spectrum in the plasma air discharge.
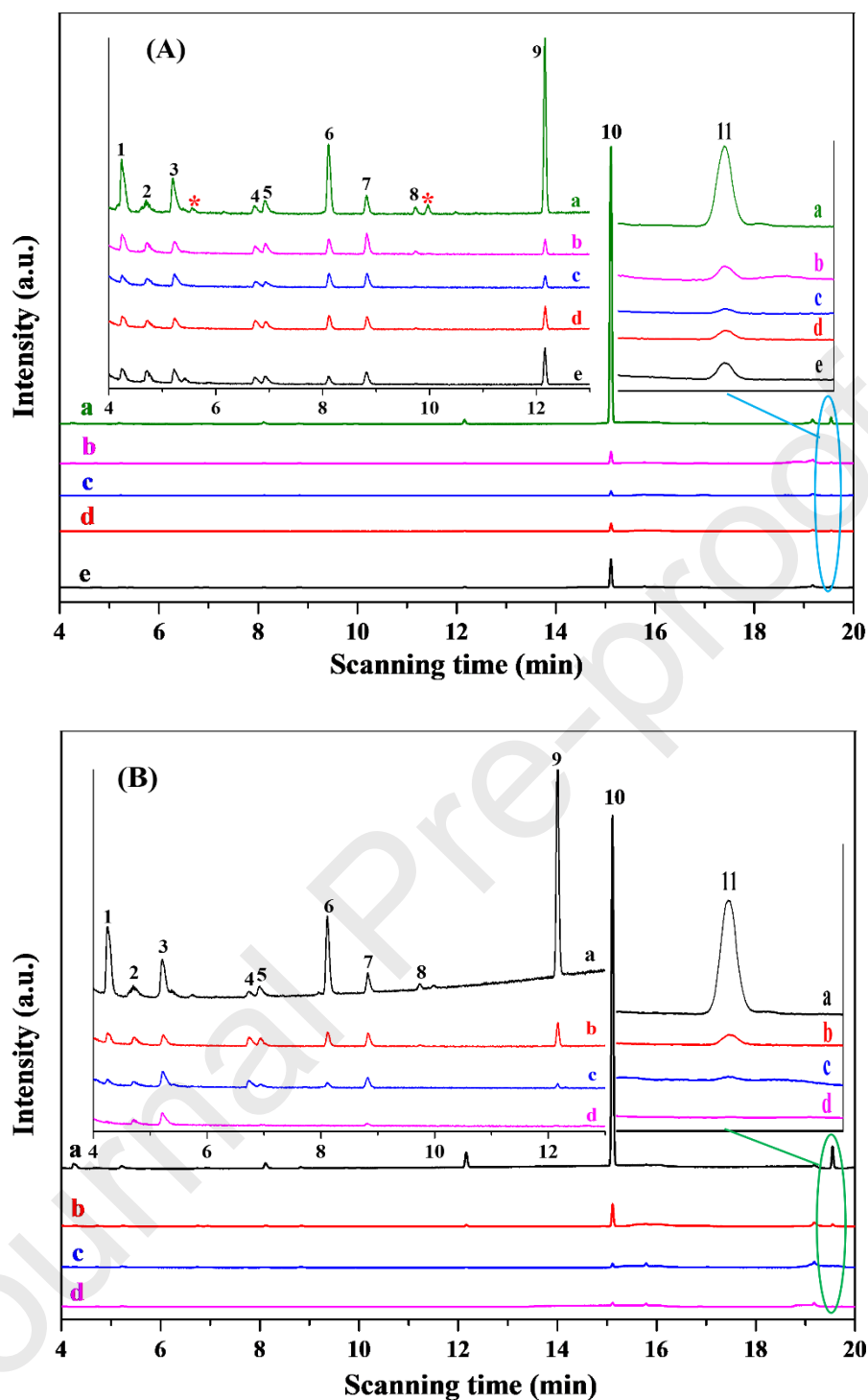
Fig. 13. GC-MS spectra of gaseous by-products in the plasma-catalysis system. (A) different catalyst (Lines a-e in order: MS, 3An:1Ru/MS, P25/MS, An/MS, Ru/MS) at 5 min; (B) different reaction time of An/MS catalyst (Lines a-d: 90 s, 5 min, 6.5 min, 30 min): (1) Methyl nitrite, (2) Acetaldehyde, (3) Ethylamine, (4) Acetonitrile, (5) Acetone, (6) Methyl nitrate, (7) Methane, nitro, (8) Acetic acid ethenyl- , (9) Benzene, (10) Toluene, (11) Benzaldehyde.
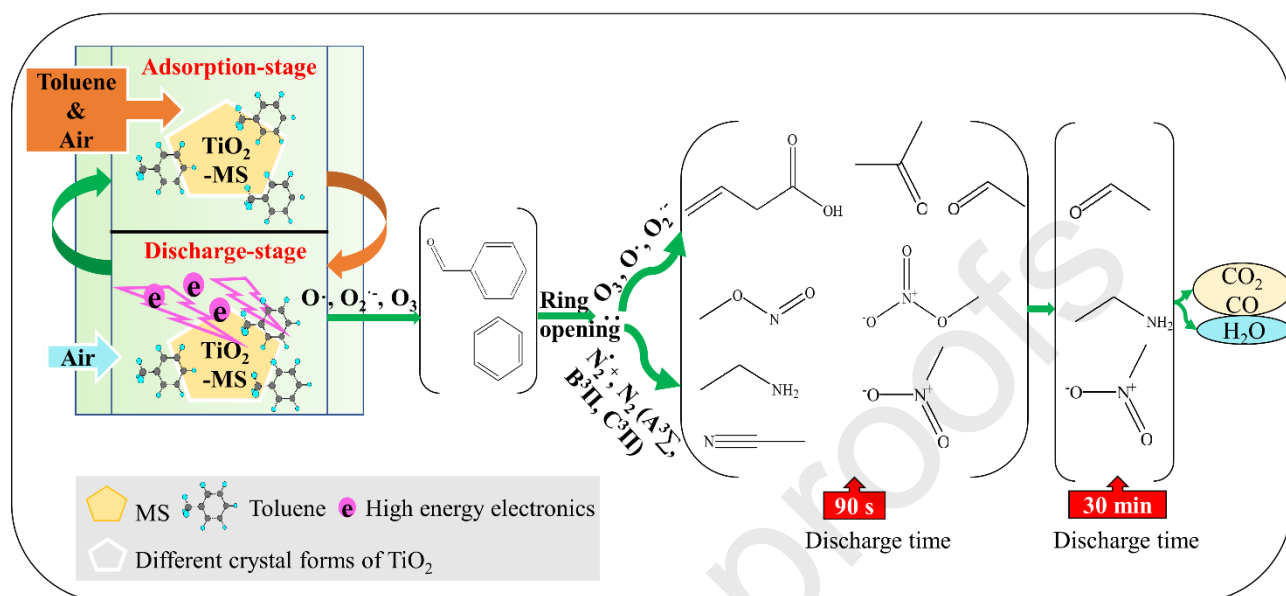
Fig. 14. The pathway of toluene decomposition in plasma-photocatalytic system.
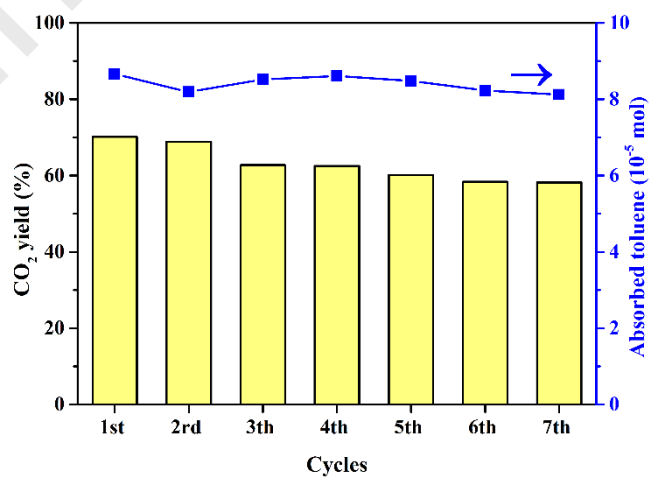

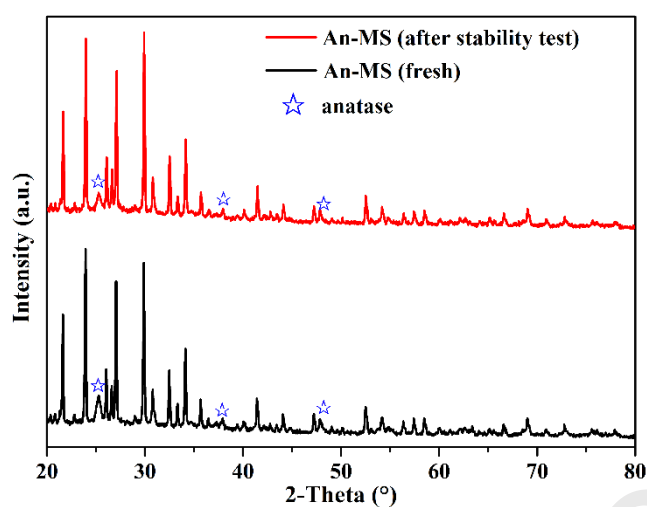
Fig. 15. Stability tests for plasma-An/MS system.

Fig. 16. XRD patterns of An/MS before and after stability test.

Table 1

Oxygen atomic percentage contents and valence state changes of Ti for various samples.

Samples	O-Ti^{4+}	O-Ti^{3+}	Sur-OH	Vacancy O	Adsorb O	Ti^{3+}/ (Ti^{3+}+Ti^{4+})	Ti^{4+}/ (Ti^{3+}+Ti^{4+})
An/MS	4.53	3.91	40.54	44.27	6.75	33.74	66.26
Ru/MS	4.61	3.95	41.63	40.32	9.49	31.82	68.18
P25/MS	4.07	3.14	42.03	44.35	6.41	34.49	65.51
3An:1Ru/MS	3.28	3.62	47.90	36.97	8.23	29.82	70.18

Table 2

Sample	Catalyst dose (g)	Toluene Adsorption Capacity (mmol)	CO_2 production amount (mmol)	Total Toluene removal efficiency (%)	CO_2 yield (%)	CO yield (%)	Space time yield (g/L/h)	Band gap (eV)	
								Direct $(\alpha h\nu)^2$ vs $h\nu$	Indirect $(\alpha h\nu)^{1/2}$ vs $h\nu$
An/MS	4.506	0.107	0.518	98.1	69.1	25.8	2.35	3.32	3.18
Ru/MS	4.509	0.104	0.462	98.5	63.5	25.6	2.09	3.10	2.98
P25/MS	4.507	0.101	0.477	99.5	67.5	22.2	2.16	3.21	3.01
3An:1Ru/MS	4.511	0.106	0.442	98.4	59.6	20.8	2.0	3.28	3.02
MS	4.506	0.105	0.289	95.3	39.3	7.0	1.31	-	-

The summaries of catalytic performances in the processes of plasma-photocatalysis.

(Toluene initial concentration: 153 mg/m³, Space velocity: 927 h⁻¹ (discharge process), 18547 h⁻¹ (adsorption process), Input power: 13.1 W,

Specific energy: 7.86 kJ/L, Adsorption time: 90 min, Discharge time: 90 min)

Sample	E field (10^{-21} Vm^2)	Te /eV (± 0.5 eV)	T_{rot} /K (± 55 K)	T_{vib} /K (± 400 K)
An /MS	525	4.2	627	2450
Ru /MS	505	3.9	648	2600
P25/MS	670	4.7	591	2216
3An:1Ru/MS	510	4.1	512	2335

based

Table 3

Electrical discharge properties obtained on OES analysis of spectral data.

Table 4

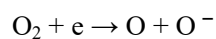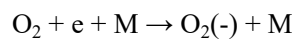Oxygen atomic percentage contents of the catalyst samples after plasma discharge.

Samples	O-Ti^{4+}	O-Ti^{3+}	Sur-OH	Vacancy O	Adsorb O
An/MS	4.14	7.47	34.00	47.91	6.48
Ru/MS	3.85	5.57	40.81	44.88	4.89
P25/MS	7.87	8.25	30.53	48.42	4.93
3An:1Ru/MS	5.16	5.94	42.80	40.87	5.23

Table 5
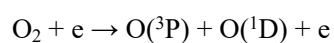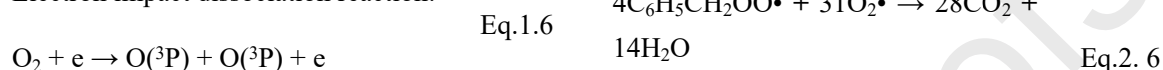
Possible reactions of plasma discharge process and photocatalytic process.

Plasma discharge process		Photocatalytic process	
$C_6H_5CH_3^+ + e^- \rightarrow C_6H_5\cdot + CH_3\cdot$	Eq.1. 1	$2O_{ads} + e^- \rightarrow O_2^{\cdot-}$	Eq.2.1
$C_6H_5CH_3^+ + e^- \rightarrow C_6H_5CH_2\cdot + H\cdot$	Eq.1. 2	$O_3 + e^- \rightarrow O_3^- \rightarrow O^{\cdot-} + O_2$	Eq.2. 2
$C_6H_5CH_2\cdot + O_2 \rightarrow C_6H_5CH_2OO\cdot$	Eq.1. 3	$C_6H_5CH_{3ads} + O_2\cdot \rightarrow C_6H_5CH_2\cdot + HO_2\cdot$	Eq.2. 3
$C_6H_5CH_2OO\cdot \rightarrow C_6H_5CHO + HO\cdot$	Eq.1.4	$C_6H_5CH_2\cdot + O_2 \rightarrow C_6H_5CH_2OO\cdot$	Eq.2. 4

51

Ionization of O_2:

$$O_2 + e \rightarrow O_2{}^+ + 2e \qquad \text{Eq.1.5}$$

$$O_2 + e + M \rightarrow O_2(-) + M$$

$$O_2 + e \rightarrow O + O^-$$

$$C_6H_5CH_2OO\bullet \rightarrow C_6H_5CHO + HO\bullet \qquad \text{Eq.2. 5}$$

Electron impact dissociation reaction:

$$\text{Eq.1.6}$$

$$O_2 + e \rightarrow O(^3P) + O(^3P) + e$$

$$O_2 + e \rightarrow O(^3P) + O(^1D) + e$$

$$4C_6H_5CH_2OO\bullet + 31O_2\bullet \rightarrow 28CO_2 + 14H_2O \qquad \text{Eq.2. 6}$$

Formation of atomic oxygen by nitrogen molecules excited by electrons:

$$\text{Eq.1.7}$$

$$N_2 (A^3\textstyle\sum) + O_2 \rightarrow N_2 (X^1\textstyle\sum) + O + O$$

$$N_2 (B^3\textstyle\sum) + O_2 \rightarrow N_2 (X^1\textstyle\sum) + O + O$$
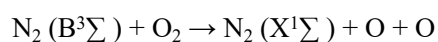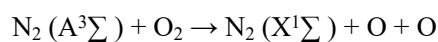
Highlights

• The effect of mixed-phase TiO_2 on adsorption-plasma photocatalytic oxidation of toluene is discussed.

• Different phases of TiO_2 affecting plasma chemistry are analyzed.

• Possible plasma-assisted photocatalytic reactions are discussed.